A STUDY ON THE STABILITY OF THE LED GAIN MONITORING SYSTEM FOR THE CMS-HF PMTs DURING 2009

by

Melih Özbek

B.S., Physics, Boğaziçi University, 2008

Submitted to the Institute for Graduate Studies in
Science and Engineering in partial fullfillment of
the requirements for the degree of
Master of Science

Graduate Program in Physics
Boğaziçi University
2010

ACKNOWLEDGEMENTS

I would like to express my gratitude to Professor Erhan Gülmez for his kind assistance with my thesis studies. His guidance proved invaluable during the preparation of this thesis.

I also thank Kerem Cankoçak and my dear friend Bora Işıldak for their help during my studies at CERN. I would also like to thank Serhat Iştın for sharing his knowledge about programming.

Finally, a special thanks goes to my dear family for their unconditional love and support since the very first day I was born, and Didem Gürsel, for her understanding and encouragement during my studies.

ABSTRACT

A STUDY ON THE STABILITY OF THE LED GAIN MONITORING SYSTEM FOR THE CMS-HF PMTs DURING 2009

The Hadronic Forward (HF) calorimeter improves the jet detection and the missing transverse energy resolution of the Compact Muon Solenoid (CMS). In HF, the Photo Multiplier Tubes (PMTs) convert optical signals (i.e., Čerenkov light) to electrical signals. For monitoring the PMT gains, LED signals are extensively used.

LED data collected throughout 2009 were thoroughly studied in this thesis. The focus was analyzing the stability of the LED system over time by graphical means. Also, by plotting the average charge versus position, it was possible to identify problematic channels.

ÖZET

CMS-HF PMT'LERİ İÇİN LED KAZANÇ İZLEME SİSTEMİNİN 2009'DAKİ KARARLILIĞI ÜZERİNE BİR ÇALIŞMA

İleri Hadronik Kalorimetre (HF), Compact Muon Solenoid (CMS)'de jet saptanması ve dik yönde kayıp enerji çözünürlüğü konusunda önemli katkı sağlar. HF'te, Foto Çoğaltıcı Tüpler (PMT'ler), ışık sinyalini (Čerenkov ışığını) elektrik sinyaline çevirir. PMT'lerin kazançlarının izlenmesi için LED sinyalleri yaygın olarak kullanılır.

Bu tezde, 2009 yılında alınmış LED verisi ayrıntılı olarak incelenmiştir. Odak noktası, grafik analizi yöntemiyle LED sisteminin kararlılığını analiz etmek olmuştur. Ayrıca, pozisyona göre ortalama yük grafikleri yardımıyla, problemli kanallar tespit edilmiştir.

TABLE OF CONTENTS

LIST OF FIGURES

LIST OF TABLES

LIST OF SYMBOLS / ABBREVIATIONS

c	Speed of light
GeV	Giga electron-volt
GJ	Gigajoule
HV	High Voltage
ieta	Eta index
iphi	Phi index
K	Kelvin
kC	Kilo Coulomb
MeV	Mega electron-volt
MHz	Megahertz
ns	Nanosecond
T	Tesla
TeV	Tera electron-volt
η	Pseudorapidity
μm	Micrometer

AVP	Avalanche Photodiode
CBOX	Calibration Box
CLI	Calibration Light Injector
CMS	Compact Muon Solenoid
CSC	Cathode Strip Chamber
DT	Drift Tube
EB	Barrel Electromagnetic Calorimeter
ECAL	Electromagnetic Calorimeter
EE	Endcap Electromagnetic Calorimeter
HB	Barrel Hadronic Calorimeter
HCAL	Hadronic Calorimeter
HE	Endcap Hadronic Calorimeter
HF	Forward Hadronic Calorimeter
HO	Outer Barrel Hadronic Calorimeter
HPD	Hybrid Photodiodes
LED	Light Emitting Diode
LEP	Large Electron Positron Collider
LHC	Large Hadron Collider
LSP	Lightest Supersymmetric Particle

MACHO	Massive Astrophysical Compact Halo Object
PMT	Photo Multiplier Tube
PS	Proton Synchrotron
QIE	Charge Integrator and Encoder
RBX	Readout Box
RF	Radio Frequency
RPC	Resistive Plate Chamber
SM	Standard Model
SPS	Super Proton Synchrotron
SUSY	Supersymmetry
TEC	Tracker End Cap
TIB	Tracker Inner Barrel
TID	Tracker Inner Disks
TOB	Tracker Outer Barrel
VPT	Vacuum Phototriodes
WIMP	Weakly Interacting Massive Particle

1. INTRODUCTION

With a center of mass energy of 14 TeV, the Large Hadron Collider (LHC) has the potential to start a new era in physics. The primary goal of the LHC is to explain the Higgs mechanism, through which all the elementary particles are thought to gain mass. The Compact Muon Solenoid (CMS) is one of the two main detectors in the LHC which is capable of studying a wide range of physics.

The Hadron Forward Calorimeter (HF) is a subsystem of the Hadronic Calorimeter (HCAL) in the CMS. Its main purpose is to detect hadronic jets and to increase the missing transverse energy resolution of the CMS. In order to calibrate and monitor the HF components, the Light Emitting Diode (LED) system is extensively utilized. During CMS operation, LED runs are regularly taken to monitor the gain stability of the Photo Multiplier Tubes (PMTs) and the Hybrid Photodiodes (HPDs), the noise, the timing and the Charge Integrator-Encoder (QIE) elements.

In this thesis, we focused on a bunch of LED runs taken in 2009. The data taken during these runs were thoroughly analyzed by graphical means. Our main motivation has been to examine the gain stability of the PMTs during the whole year and also to identify the problematic channels in HF.

The thesis begins with a short explanation of the LHC. The design and the goals of the CMS are discussed in the following chapter. We briefly explained the CMS Hadronic Calorimetry in chapter four. A general presentation of the HF can be found in the next chapter, where the focus of this thesis, the LED system, is also explained, along with the PMTs. In chapter six, the analysis regarding the 2009 LED data is presented, which is succeeded by a conclusion of our results in the last chapter.

2. THE LARGE HADRON COLLIDER

With an unsurpassed center of mass energy of 14 TeV, the Large Hadron Collider (LHC) is the largest particle accelerator in the world. The main goal of the LHC is the search for the Higgs boson, a massive elementary particle predicted by the Standard Model, which is thought to be responsible for electroweak symmetry breaking. All elementary massive particles are thought to gain mass via this mechanism. Despite the fact that the Standard Model gives precise results at low energies, it is quite likely that it might only be a part of a more fundamental theory. Hence, to complement the SM, new ideas are brought about, namely extra dimensions, supersymmetry (SUSY), technicolor, dark matter, etc. Of course, a currently unpredicted mechanism is also possible.

2.1. Design and Construction

The LHC is located on the Franco-Swiss border, near Geneva. The 26.7 km long LHC tunnels were built between 1984 and 1989 for the Large Electron Positron Collider (LEP). Depending on the geometry of the surface, the tunnels of the LHC lie at a depth varying from 50 to 175 meters. The LHC has the potential of colliding bunches of 10^{11} protons at 40 million times per second at a luminosity of 10^{34} cm^{-2} s^{-1} .

Table 2.1. The machine parameters for the LHC detectors

	pp	**HI**
Energy per nucleon (TeV)	7	2.76
Dipole Field at 7 TeV (T)	8.33	8.33
Design Luminosity (cm^{-2} s^{-1})	10^{34}	10^{27}
Bunch separation (ns)	25	100
Number of bunches	2808	592
Number of particles per bunch	$1.15x10^{11}$	$7.0x10^{7}$

(pp : proton-proton collisions. HI: heavy ion collisions.)

There are four main detectors located in the LHC : CMS, ATLAS, LHCb and ALICE. Additionally, the two relatively smaller detectors, TOTEM and LHCf, are located near CMS and ATLAS, respectively. As mentioned above, some parts of the LHC were actually constructed for the LEP, and are still being used effectively. The ALICE and LHCb caverns have been being used since the LEP, whereas those of ATLAS and CMS are relatively new. ATLAS and CMS are high luminosity experiments, and they will shed light on many subjects in physics, the most important of which will be the hunt for the Higgs boson. LHCb and TOTEM, which are two low luminosity experiments, will analyze bottom quarks and protons from elastic scattering, respectively. ALICE, on the other hand, will be working with heavy ions.

There are eight arcs and eight straight parts in the LHC. In the straight sections, which are each 528 m long, the particles can be injected into the tunnels, cleaned, or dumped. There are bending dipole magnets in the arcs. The CMS experiment is located at Point 5 and the ATLAS experiment is located at Point 1.

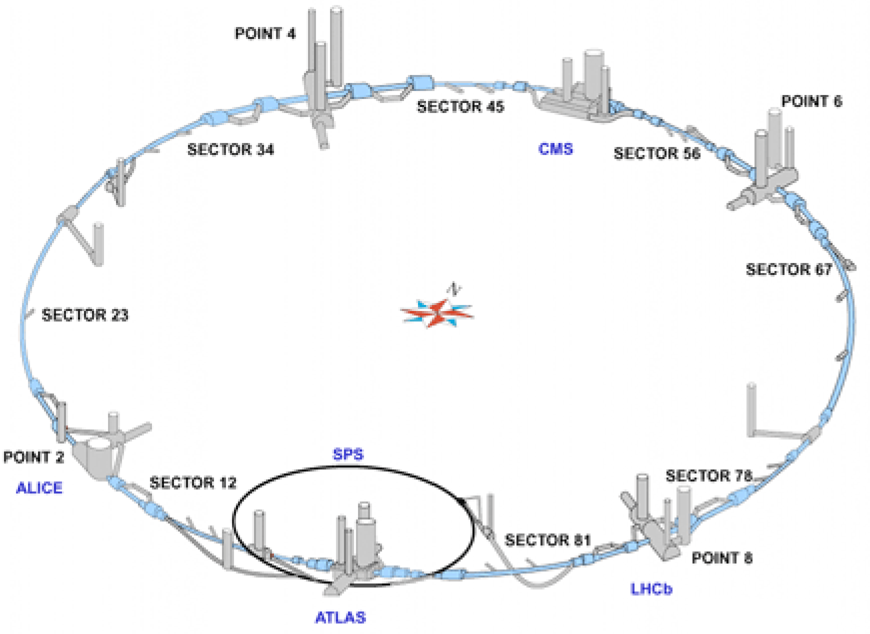

Figure 2.1. General view of the Large Hadron Collider

2.1.1 The Beam

Before the proton beams are injected to the LHC, they go through several accelerators. After being extracted from ionized hydrogen, protons are first accelerated to 50 MeV in

Linac 2. Subsequently, the Proton Synchrotron Booster accelerates the particles to 1.4 GeV, and transfer the protons to the Proton Synchrotron (PS), where the particles reach an energy of 26 GeV, with 25 ns spacing. Afterwards, the Super Proton Synchrotron (SPS) accelerates the bunches to 450 GeV, and then they are injected into the LHC. For each opposing beam, this process has to be repeated twelve times.

The beam consists of numerous bunches of protons, piled up along a line, one after another. In 75 ns operation, each beam will have 936 bunches, whereas a 25 ns spacing translates into 2808 bunches for each beam [1]. Theoretically, 25 ns spacing is a frequency of 40 MHz, but a gap is needed for the rise time of the dump kickers, hence the actual frequency is slightly less than that. The opposing beams circulate through beam pipes, which are held constantly in vacuum. The protons are accelerated and kept together as bunches with the help of the superconducting RF cavities operating at 4.5 K. At interaction points, the opposing beams are aligned in order to observe collisions. The beam pipes also serve as absorbers for residual particles.

The LHC contains numerous magnets of different types. A few examples are main dipoles, lattice quadrupoles, lattice sextupoles, lattice octupoles, skew quadrupoles etc. [2] Among the magnets, the 1232 superconducting main dipole magnets give the high energy LHC beams the circular shape. Since the machine radius is not a parameter that can be adjusted, the magnetic field has to be increased as the energy rises, eventually the dipoles will have to produce a field of about 8.33 Tesla as the 7 TeV energy per beam is achieved. The superconducting magnets operate at about 1.9 K. They are completely filled with helium, and such low temperatures are well known to be a necessity for superconductivity. The beam pipes through which the particles circulate are encapsulated by the magnets.

2.2 Current Status

The LHC started commissioning on 10 September 2008, with a successful 450 GeV pilot run, which took about an hour. However, due to helium leak from supermagnets in sector 3-4, the LHC went temporarily offline for repairs. More than a year later (on 20

November 2009), the proton beams began to circulate again. Only ten days later, the LHC became the world’s highest-energy particle accelerator, when two 1.18 TeV beams successfully collided. At the time this thesis is being written, two proton beams, having an energy of 3.5 TeV each, successfully circulate in the Large Hadron Collider; thus carrying the world record of the beam with the highest energy one step forward. 7 TeV collisions started on 30 March 2010. After observing the 7 TeV collisions, the plan is to keep the beam on for 18-24 months, with a short stop for maintenance at the end of 2010 [3].

3. THE COMPACT MUON SOLENOID

Having a large spectrum of research prospects, the Compact Muon Solenoid (CMS) is one of the two main detectors in the LHC. The CMS has an overall diameter of 14.6 m, a length of 21.5 m, and a total weight of 12500 tons. A 4T superconducting solenoid is placed inside. The main reason for providing this strong magnetic field is to help increase the momentum resolution.

The CMS adopts a coordinate system in which the origin is the interaction point, the z axis points along the beam, the x axis points radially inward toward the center of the LHC, and the y axis points vertically upward. The azimuthal angle ϕ is measured from the x axis in the x-y plane. The polar angle θ is measured from the z axis. Instead of using the plain polar angle θ, pseudorapidity is preferred, defined as $\eta = -\ln\tan(\theta/2)$.

3.1. Design

The CMS consists of several layers, namely, the silicon tracking system, the electromagnetic calorimeter (ECAL), the hadronic calorimeter (HCAL), the superconducting solenoidal magnet and the muon chambers separated by the return yoke system.

3.1.1. The Silicon Tracker

The silicon tracker, covering a pseudorapidity range of $-2.4 < \eta < 2.4$, can reconstruct the trajectories of the particles. The momentum of the particles can be calculated by analyzing the curvature of the trajectories.

The strip tracker and the pixel tracker together form the whole tracking system. The strip tracker is made up of Tracker Inner Barrel (TIB), Tracker Outer Barrel (TOB), Tracker Inner Disks (TIDs) and the Tracker End Cap (TEC). The so-called “stereo” modules are in the first two rings of the TID and in a total of three rings of the TEC. The thickness of the sensors is 320 μm for the TID and the three inner rings of the TEC, and 500 μm for the other parts of the TEC. There are about 15400 modules in the entire silicon strip detector.

In the pixel tracker, there are three barrel layers with two endcaps. The mean radii of the layers are 4.4 cm, 7.3 cm and 10.2 cm and their length is 53 cm. Each pixel has a size of 100 x 150 μm^2 and there are a total of 65 million pixels. Using the information from the whole silicon tracker, 3-D pictures of particle trajectories can be reconstructed.

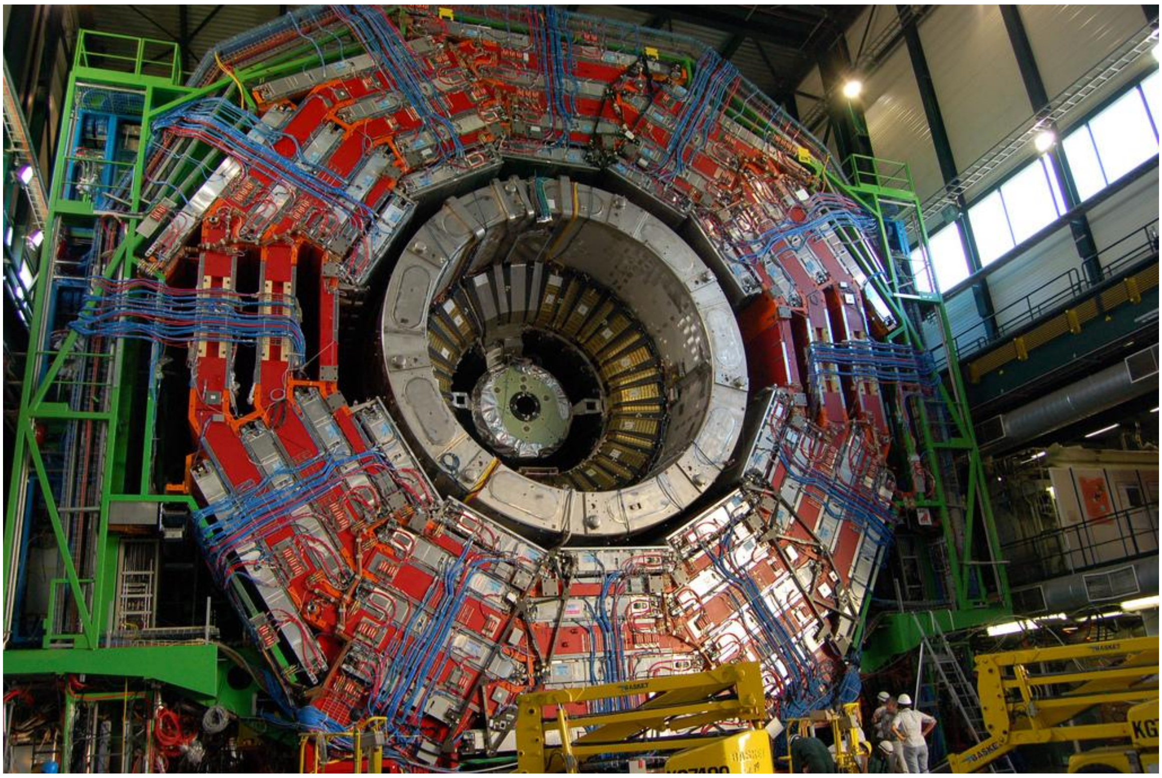

Figure 3.1. Part of the CMS detector in the cavern

3.1.2. The Electromagnetic Calorimeter

The Electromagnetic Calorimeter (ECAL) is a homogeneous calorimeter which has 61200 lead tungstate ($PbWO_4$) crystals built in its barrel part, and 14648 crystals in the two endcaps. These radiation resistant crystals have a fast response and provide a fine granularity.

The barrel section (EB) has a pseudorapidity interval of $0 < |\eta| < 1.48$. The crystals cover 0.0174 in $\Delta\eta$ and $\Delta\phi$. Its inner radius is 129 cm. In EB, Avalanche Photodiodes (AVPs) are used as photodetectors, which capture the scintillation lights coming from the crystals. The endcaps (EE), covering $1.48 < |\eta| < 3.0$, comprise semi-circular aluminium plates. The endcap crystals are identical and have a cross section of 28.6 x 28.6 mm^2 and a length of 220 mm. A preshower device covers much of the endcap pseudorapidity interval. In EE, Vacuum Phototriodes (VPTs) are used as photodetectors.

3.1.3. The Hadronic Calorimeter

A detailed explanation of the Hadronic Calorimeter (HCAL) can be found in the next chapter.

3.1.4. The Magnet

CMS contains a huge superconducting solenoidal magnet which weighs 12000 tonnes. It has dimensions of 12.9 m in length and 5.9 m in diameter. A maximum energy of 2.6 GJ can be stored in the magnet.

The properties of the magnet are determined by the muon detection process. A powerful magnet directly translates into a high bending power, and moreover, a momentum resolution $\Delta p/p \approx 10\%$ is necessary for the correct determination of the sign for muons having a momentum of ≈ 1 TeV/c.

3.1.5. The Muon System

Muon detection is a very important tool for the CMS. For example, one of the predicted decay modes of the Standard Model Higgs boson is into ZZ or ZZ*, which afterwards decay into four muons. Among leptons, muons are relatively easier to detect, and they are less affected by the radiative losses in the tracker.

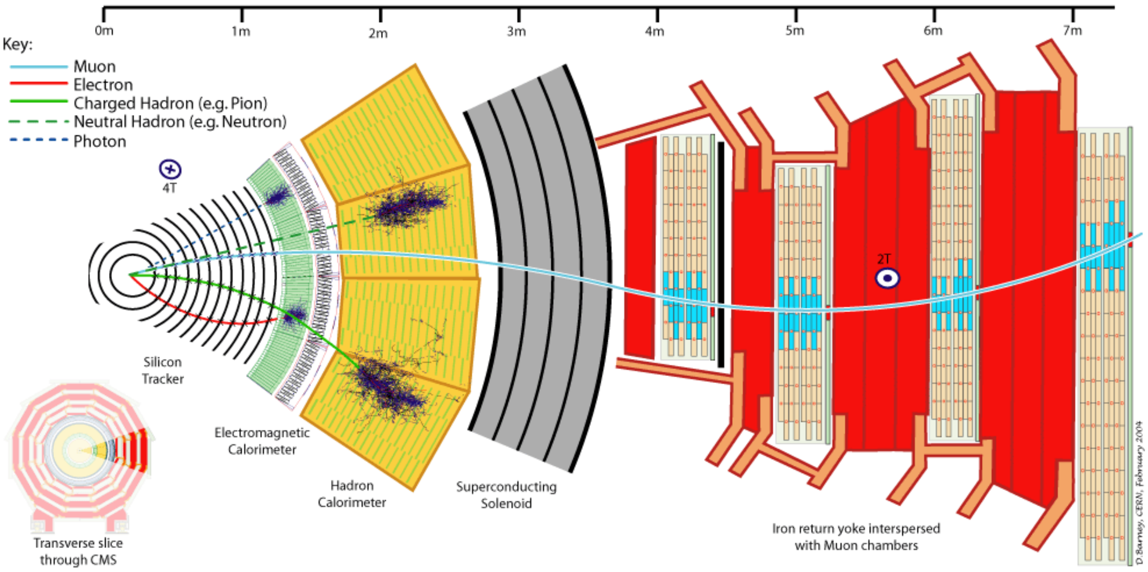

Figure 3.2. The layers of CMS

Apart from the identification of muons, the CMS muon system can also determine their momentum and charge. For muon identification, three types of gaseous particle detectors are used [4]. The muon system has a cylindirical barrel section and two planar endcap regions. In the barrel part, Drift Tubes (DTs), covering a pseudorapidity interval of $|\eta| < 1.2$, are responsible for muon position measurement. In endcap regions, Cathode Strip Chambers (CSCs) are utilized. Resistive Plate Chambers (RPCs) are located in both regions.

3.2. CMS Goals

The CMS covers a large spectrum of physics phenomena. The main motivation is to investigate the Higgs mechanism, which is presumed to be responsible for electroweak symmetry breaking. Also, there are other important subjects for the CMS, such as supersymmetry, extra dimensions and dark matter.

3.2.1. Discovery of the Higgs Boson

Higgs mechanism is thought to be responsible for the process of gaining mass for all elementary particles. After being theorized in 1964, the Higgs mechanism gained a wider recognition when Steven Weinberg and Abdus Salam applied the ideas to the electroweak symmetry breaking. In the standard model, one can mention the neutral and charged components of the Higgs field. The charged component consists of the Goldstone boson, which are related to W and Z bosons. The neutral component, on the other hand, translates into the Higgs boson. It is also possible that there exist many Higgs particles, instead of the Higgs boson being unique [5].

The Standard Model does not predict the mass of the Higgs boson. However, LEP had provided us with a lower limit, which is 114.4 GeV/c^2. In the interval between 114.4 - 130 GeV/c^2 , the decay of the Higgs particle to two photons is the principal channel. For the mass being slightly larger than 130 GeV/c^2, a decay into two Z bosons looks most promising. For masses higher than that, but smaller than 600 GeV/c^2, a final state with four leptons is the expected channel, for which the muon system in the CMS can play a significant role for detection. In the region with even higher masses, we expect to see final states that contain W and Z bosons, jets and also missing transverse energies (It might be a good point here to state that the longitudinal missing energy is impossible to measure directly, in view of the high energy particles produced in the beam pipe). The HCAL can detect these channels.

3.2.2. Supersymmetry

Supersymmetry (SUSY) is a theory which assumes that all elementary particles are related to other supersymmetric particles, the so-called “superpartners”. The spins of the related particles differ by one half. In other words, fermionic particles have superpartners that are bosonic, and vice versa (Figure 3.3). The superpartners either take an “s” in the beginning of the word, or they end with “ino”, depending on whether they are superpartners of fermions, or bosons, respectively.

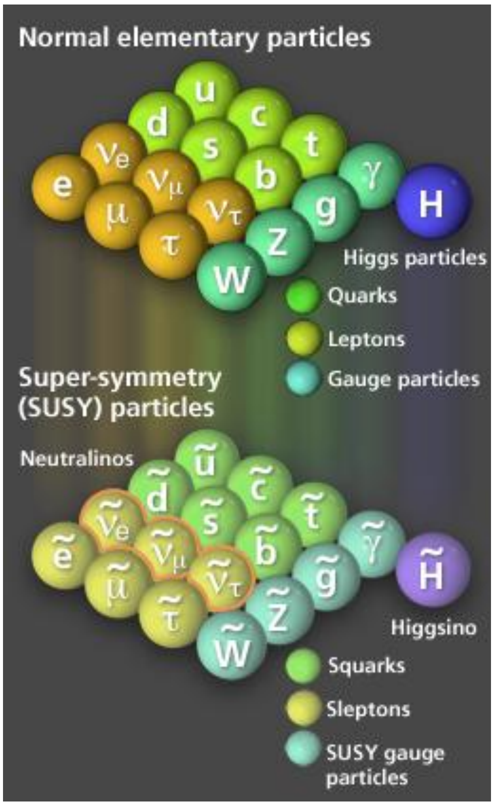

Figure 3.3. Normal elementary particles and SUSY particles

If evidence of supersymmetry is found at TeV scale (which is accessible experimentally by the LHC), it may help explain the unification theory at energies lower than expected. It is essential that the decay products of the supersymmetric particles contain cascades and always the lightest SUSY particle (LSP). Since the LSP is expected to interact weakly, it will be impossible to directly observe it. However, a significant transverse missing energy may turn out to be an indirect proof for the existence of supersymmetry.

3.2.3. Dark Matter

Following Fritz Zwicky's initial observations [6], [7] the dark matter subject gained popularity after Vera Rubin investigated the velocity of the spiral galaxies in the late 1960s and the early 1970s. They had gotten a striking result: The velocity curve of the spiral galaxies did not obey the expected Newtonian behavior (Figure 3.4) [8], [9].

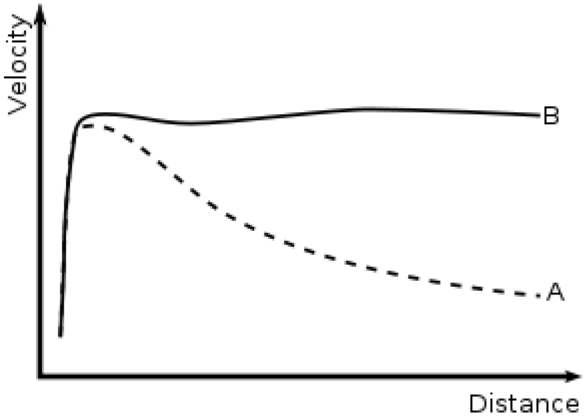

Figure 3.4. Velocity versus distance curve for spiral galaxies, according to Vera Rubin's studies: the predicted curve (A) and the observed one (B)

This observation showing that the velocity stays more or less constant with varying distance suggests that there is some extra matter we cannot perceive. Dark matter studies are still continuing, by examining various phenomena such as intergalactic gas and gravitational lensing. Another popular research area is the identification of dark matter candidate particles, e.g. WIMPs (weakly interacting massive particles) and MACHOs (Massive Astrophysical Compact Halo Objects) [10]. The CMS will be mainly searching for neutralinos (which are under the WIMP group) and LSPs.

4. CMS-HCAL CALORIMETRY

4.1 Calorimetry

Calorimetry is one of the most important detection mechanisms in particle physics. Originally used for the study of cosmic rays, the calorimetry techniques have been developed for high energy particle physics experiments in order to measure the energy of electrons, hadrons and photons, as well as to identify the particles.

In the calorimetry process, the incident particles are fully absorbed. One observes a shower of secondary particles via the interaction between the detector and the incident particles. This shower, in turn, may produce tertiary particles, and so on, with degrading energies. Subsequently, the energy of the charged particles in the shower may be detected by analyzing the collected charge or light, and eventually, one may determine the energy of the incident particle.

In the area of particle physics, calorimeters offer many advantages. They can detect both neutral and charged particles. The relative energy resolution σ / E is proportional to $\sqrt{E}$ for calorimeters, which is surely an advantage when dealing with high energy particles, which is always the case in the LHC. Finally, the different responses to muons, electrons and hadrons help identify the particles.

There are two basic classifications for calorimeters. They can be either sampling calorimeters or homogeneous calorimeters. In sampling calorimeters, alternating layers of absorbers made of dense material are responsible for generating showers, and a signal is produced from an active medium. On the other hand, the tasks of signal generation and the absorption of the incident particles are done by the same parts in homogeneous calorimeters [11]. Calorimeters can also be classified as electromagnetic calorimeters (e.g. ECAL, mentioned in the preceding chapter) and hadronic calorimeters (e.g. HCAL).

4.2. Design

The design of the Hadronic Calorimeter (HCAL) is such that it encapsulates the ECAL. It lies radially between the borders of the electromagnetic calorimeter (r = 1.77 m) and the magnet (r = 2.95 m). The HCAL is responsible for identifying and also measuring the energy of the particles via various detection mechanisms. In HE, HO and HB, Hybrid Photodiodes (HPDs) convert the scintillation light that comes from the fibers to electric signal for read-out. HF has different characteristics. In the HCAL, QIEs (Charge Integrator and Encoder), consisting of four capacitors running alternatively in 25 ns time slices, are responsible for converting analog signals to digital.

4.2.1. Hadron Barrel

The Barrel Hadron Calorimeter (HB) is a sampling calorimeter having dimensions of nine metres in length, one meter in thickness and six metres in outer diameter. It covers the pseudorapditiy range of $|\eta| < 1.4$. The HB is divided into two half barrel sections with 18 identical 20^{o} ϕ wedges, which are built out of 15 brass absorber plates (built from 70% copper and 30% zinc). The total number of towers in the HB is 2304.

4.2.2. Hadron Outer

The Hadron Outer (HO) has 10 mm thick scintillators and cover the region $|\eta| < 1.3$. The main purpose of the HO is to provide extra containment region for hadron showers, as EB and HB are somewhat lacking at this process. Outside the vacuum tank of the solenoid, there are five 2.54 m wide (along z axis) rings. The HO is located as the first layer in each of these rings. It consists of several layers of scintillator tiles positioned in front of the barrel muon detector. The most important contribution of the HO is to significantly decrease the leakage (by acting as a tail catcher) and improve the missing transverse energy measurement, which is crucial for the search of supersymmetric particles.

4.2.3. Hadron Endcap

The Hadron Calorimeter Endcaps (HE) cover an important part of the pseudorapidity range ($1.3 < |\eta| < 3.0$). HE and HB are both made of brass and scintillator. They also have the same segmentation, which is of the size $\Delta\eta$ x $\Delta\phi$ = 0.087 x 0.87, except when $|\eta|$

is about 3.0, where the segmentation size is doubled. The total number of towers is again 2304. Since the HE covers about 13% of the solid angle, and also in view of the high luminosity of the LHC, it has to be highly resistant to radiation, especially at regions with high eta values. Also, it has to be able to contain hadronic showers, and should have good mechanical properties and it should be non-magnetic, since it is placed in a 4 T magnet. In view of these arguments, it is easy to understand why brass was preferred in HE.

4.2.4. Hadron Forward

The details of the hadron forward calorimeters are discussed in the following section.

5. HADRON FORWARD CALORIMETER

The Hadron Forward (HF), which was lowered into the CMS experimental cavern in 2006, covers a large pseudorapidity range of $3.0 < |\eta| < 5.0$. The HF improves jet detection and the missing transverse energy resolution capabilities of the CMS, which is very important for the discovery of the Higgs boson and supersymmetric particles. The HF calorimeters are designed to detect high energy jets with a high precision (20 to 30% at 1 TeV) during its estimated lifetime of 10 years.

The forward calorimeter is a steel cylinder, with an outer radius of 130.0 cm. The whole structure is divided into 20 degrees of azimuthal segments. There are 18 wedges on each calorimeter, HF+ and HF-. The fibers are parallel to the beam axis. They are grouped into "towers" of size $\Delta\eta \times \Delta\phi = 0.0175 \times 0.175$ (Figure 5.1). The detector is shielded from radiation with dense materials and an additional plug in the back. Furthermore, the PMTs are shielded with steel-lead-polyethylene material, so that they are not affected by the strong magnetic field within the HCAL and the radiation coming from the collisions.

In HCAL, towers are indexed according to their η (pseudorapidity) and ϕ (azimuthal angle) intervals. Mid-point η and ϕ values are integerized and used as ieta and iphi indices. In HF, ieta ranges from 29 to 41 (Table 5.1). On the other hand, the angle ϕ is divided into iphi towers that range from 1 to 71 in steps of two.

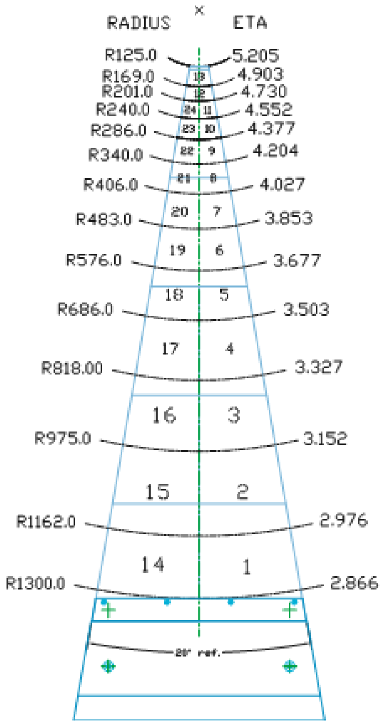

Figure 5.1. The HF tower structure

5.1. Detection Mechanism

If a charged particle passing a medium possesses a velocity higher than that of light in that medium, an electromagnetic phenomenon called Čerenkov Radiation occurs. The particle loses some energy and a bluish light is observed. By analyzing the intensity and the angle of the radiation, one can determine the velocity of the particle. The identification of the particle is also possible, provided that the momentum of the particle is known. In HF, charged shower particles exceeding the Čerenkov threshold generate Čerenkov light. Subsequently, the signal travels through the light guides to the PMTs. Only a fraction of the generated light is transmitted to air-core light guides through the fibers.

Figure 5.2. HF wedges with fibers inserted into the steel absorber

The two forward calorimeters (HF+ and HF-) placed on opposite ends of the CMS are made of quartz fibers placed inside iron. The main reason of using quartz (silicon and hard polymer) is to resist the strong radiation which results from the high luminosity, especially at $|\eta| \approx 5$. Two sets of fibers are attached into the holes on the 5 mm thick steel absorber plates. Half of the fibers extend over the full depth of the absorber (165 cm) while the other half starts at a depth of 22 cm. The signals coming from these fiber sets are read out separately. The motivation behind this classification was to distinguish the showers coming from electrons and photons (whose energy is mostly absorbed in the first 22 cm) and hadrons, which produce signals along both sets of fibers. As a convention, the fibers extending over the full depth are called “long fibers” and the fibers that start at a depth of 22 cm are called “short fibers” (referred to as “Depth 1” and “Depth 2” in this thesis, respectively). In the holes, a long fiber is succeeded by a short fiber, and vice versa.

5.1.1. Photo Multiplier Tubes

The Photo Multiplier Tubes (PMTs) used in HF were chosen and tested at the University of Iowa test station [12], [13], [14]. Hamamatsu R7525 PMTs are used in the HF. There are 864 PMTs on each side of the HF. They are grouped into 36 RBXs with 24 PMTs each. Thus, each RBX covers 10 degrees in azimuth. The PMTs were separated into three groups according to their gains. The gains are typically in the order of 10^5. PMTs with low gains were placed closer to the beam (which corresponds to high eta values). The main reason for this is due to the high energy particles being closer to the beam. About 1kC of charge is supposed to accumulate during the operation time (about 10 years).

Table 5.1. Sizes of the HCAL readout towers in η and ϕ

Tower index (ieta)	η range		Size	
	Low	High	η	ϕ
29	2.853	2.964	0.111	10
30	2.964	3.139	0.175	10
31	3.139	3.314	0.175	10
32	3.314	3.489	0.175	10
33	3.489	3.664	0.175	10
34	3.664	3.839	0.175	10
35	3.839	4.013	0.174	10
36	4.013	4.191	0.178	10
37	4.191	4.363	0.172	10
38	4.363	4.538	0.175	10
39	4.538	4.716	0.178	10
40	4.716	4.889	0.173	20
41	4.889	5.191	0.302	20

In order not to exceed 1kC, theoretically, the PMT gain must be about $5\text{x}10^4$ for the region closest to the beam (with high pseudorapidity), $1.5\text{x}10^5$ for the middle region, and $5\text{x}10^5$ for the furthest region (low pseudorapidity). During the calibration of the PMTs under different HV values, a calibration error of about 3% was obtained. This error increases for low gain PMTs.

5.2. LED System

There are three hardware systems that are being used for the calibration and monitoring of the HF: Laser Gain Monitor, Light Emitting Diodes and Moving Radioactive Sources. During test beam studies, the PMTs that are used today were tested with electron, pion and muon beams. Furthermore, LED runs were taken in order to determine the gains of the PMTs, as well as the dependence of the gains on the high voltage applied on the PMTs. During the LHC operation, regularly taken LED runs are necessary to monitor the gain stability of the PMTs and the HPDs, the amount of noise in the system, the QIE elements and the timing. The light monitoring system of the HF has three levels (Figure 5.3) [15]:

1. 1—4 (level1) UV laser light splitter
2. 1—9 (level2) Calibration Box (CBOX) laser and LED light splitter
3. 1—24 (level3) Calibration Light Injector (CLI) into PMTs.

Each CBOX has nine outputs in order to provide light to nine RBXs for each HF quadrant. The process of transporting light from a CBOX to a RBX is done with fibers. With the help of a lens, Calibration Light Injectors (CLIs) convert the calibration light into a uniform light beam. Inside the CBOX, two blue LEDs can make pulses at high rates.

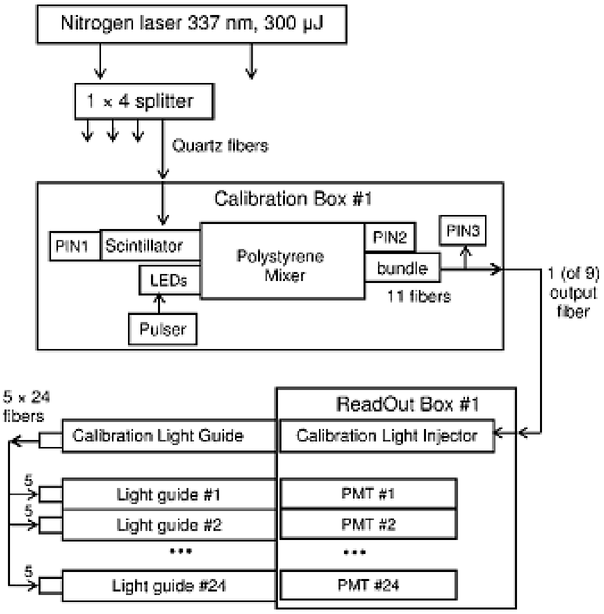

Figure 5.3. Block diagram of the LED and laser monitoring system

6. DATA ANALYSIS

The data taken during the LED runs in 2009 were analyzed by plotting the energy values as a function of time, *ieta* and *iphi* values (Table 5.1). For simple plots, Excel 2007 was used, while the three-dimensional plots were generated by ROOT. A python file available under the HCAL DQM archive (Hcal_dqm_sourceclient-file_cfg.py) was used to generate the outputs from raw data. A sample plot is shown in Figure 6.1. Throughout the analysis, the mean values of such plots were used. The data from each run were exported to excel files and were subsequently analyzed.

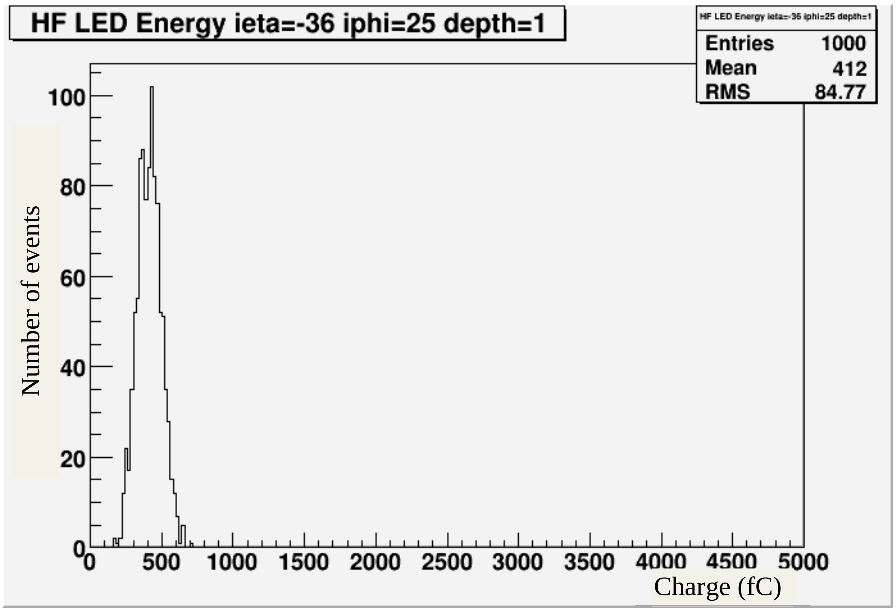

Figure 6.1. LED energy of channel ieta – iphi: 36/25, long fibers for run 101915

It was clear that the data before and after April 8, 2009 (run 81146) contained a serious shift in the energy : For all channels, the energy (throughout this thesis, wherever energy is mentioned for an LED channel, it actually means the total collected charge) suddenly dropped after the mentioned date. For some of the channels (e.g. *ieta / iphi* : 29/53, 34/43, 41/27), the energy was even halved. This observation led us to think that a major hardware change should have happened during March-April. According to the electronic logbook, the HF LED power supply was replaced on April 8. This should be the reason for the shift mentioned above. Therefore, the runs taken until April 8 were discarded after the first part of the analysis.

For the final part of the analysis, realizing that the data taken on and after September 23 had serious energy fluctuations, the runs taken during this period were also discarded. In the final analysis, 12 runs between April 22 and July 1 were used.

Table 6.1. LED Runs

Run #	**Date**	**Time of Day**	**Time of Year (Minutes)**
79172	27 March 2009	08:55	124375
79173	27 March 2009	08:58	124378
80792	7 April 2009	12:50	140450
81146	8 April 2009	18:30	142230
82317	22 April 2009	10:51	161931
82552	23 April 2009	23:00	164100
84134	07 May 2009	09:11	183431
84187	07 May 2009	19:03	184023
96151	13 May 2009	11:51	192231
96240	14 May 2009	11:21	193641
96288	14 May 2009	20:14	194174
97037	19 May 2009	23:31	201571
97582	27 May 2009	09:00	212220
98059	2 June 2009	12:24	221064
98119	2 June 2009	15:27	221247
101915	1 July 2009	20:43	263323
114198	23 September 2009	02:18	383178
114865	27 September 2009	01:28	388888
114879	27 September 2009	03:26	389006
114893	27 September 2009	05:22	389122
118846	29 October 2009	12:09	435609
121679	19 November 2009	15:30	466050
121681	19 November 2009	12:00	465840

6.1. ROOT

ROOT is an object-oriented data analysis program written in C++ at CERN. Realizing that the old FORTRAN libraries had reached their potential and considering the huge amount of data the Large Hadron Collider is to bring about, ROOT was developed in the mid 1990’s. It is mainly used for data analysis and data acquisition, as well as histogramming, curve fitting, three-dimensional visualizations, event generation etc. [16]

6.2. Analysis

The data taken from local LED runs in 2009 were categorized by depth (in view of different read-outs from the separate long and short fibers) and by the sign of pseudorapidity (eta), i.e., HF+ or HF-.

First of all, ten randomly selected channels were analyzed (Figures 6.2 and 6.3).

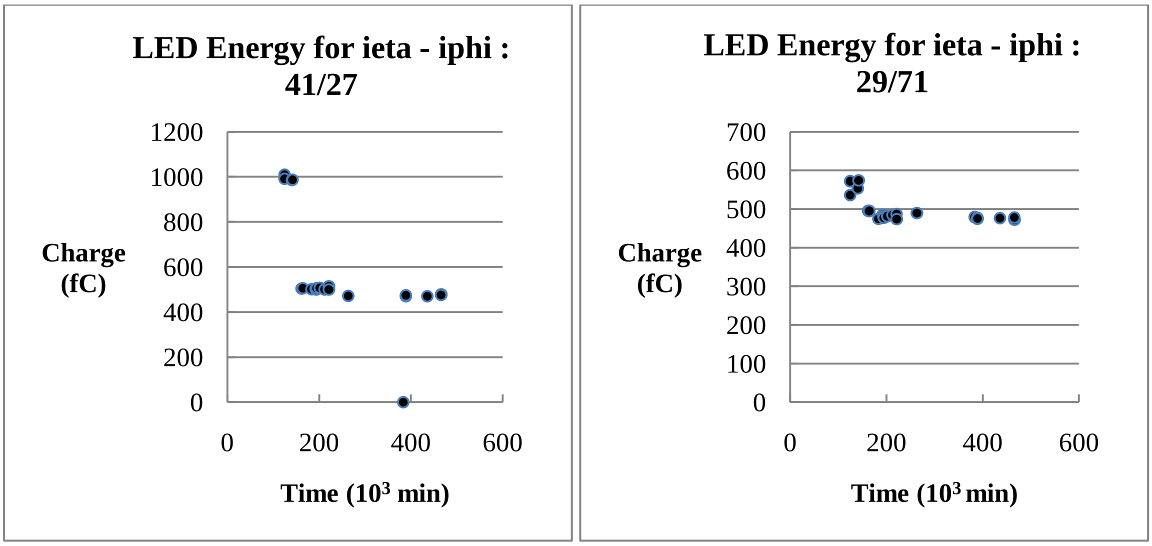

Figure 6.2. Energy distribution of channel 41/27 (depth 1) and 29/71 (depth 2) throughout 2009

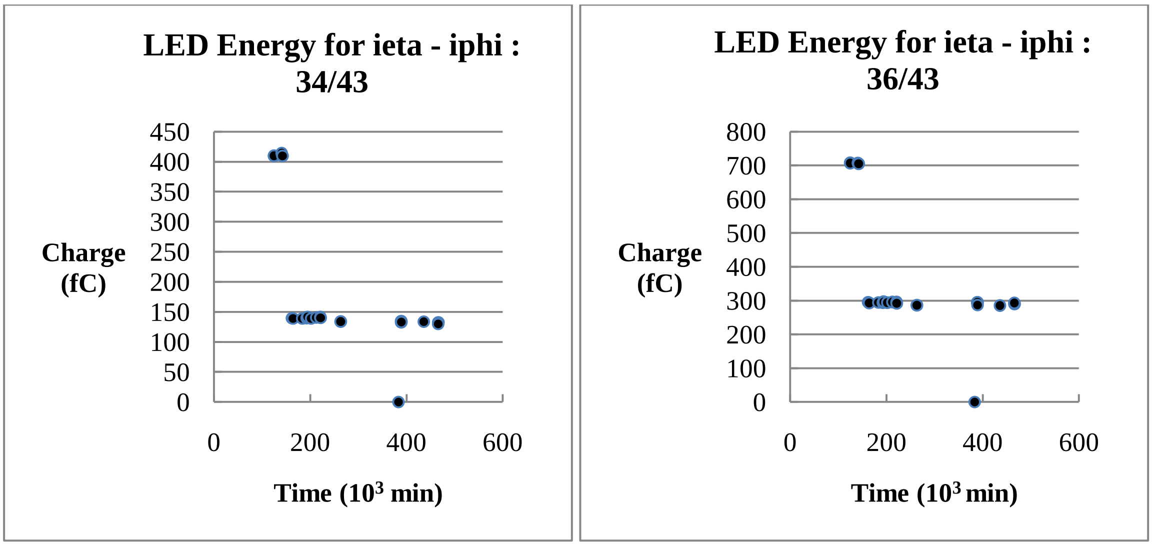

Figure 6.3. Energy distribution of channel 34/43 (depth 2) and 36/43 (depth 1) throughout 2009

For consistency, the first four runs, which are the runs on and before April 8, were discarded for the rest of the analysis. According to the electronic logbook, there had been minor hardware changes affecting the whole detector throughout the year, we decided to select a reference channel for each depth in order to remove the fluctuations caused by these changes.

The behavior of all of the channels with respect to the reference channels (“Relative Energy”) was analyzed in detail. For depth 1, the channel -29/33 was selected as the reference channel, since the fluctuations in the energies in this channel were smaller, compared to the other channels. Similarly, for depth 2, -41/31 was chosen. Both reference channels are located in HF-.

For the rest of the analysis, the data were divided into four groups : HF plus / minus and Depth 1 / Depth 2. By taking the ratio of the mean energy of each channel (for all runs) to the reference channels, the relative mean energy results were calculated. We obtained the following results for the relative energies :

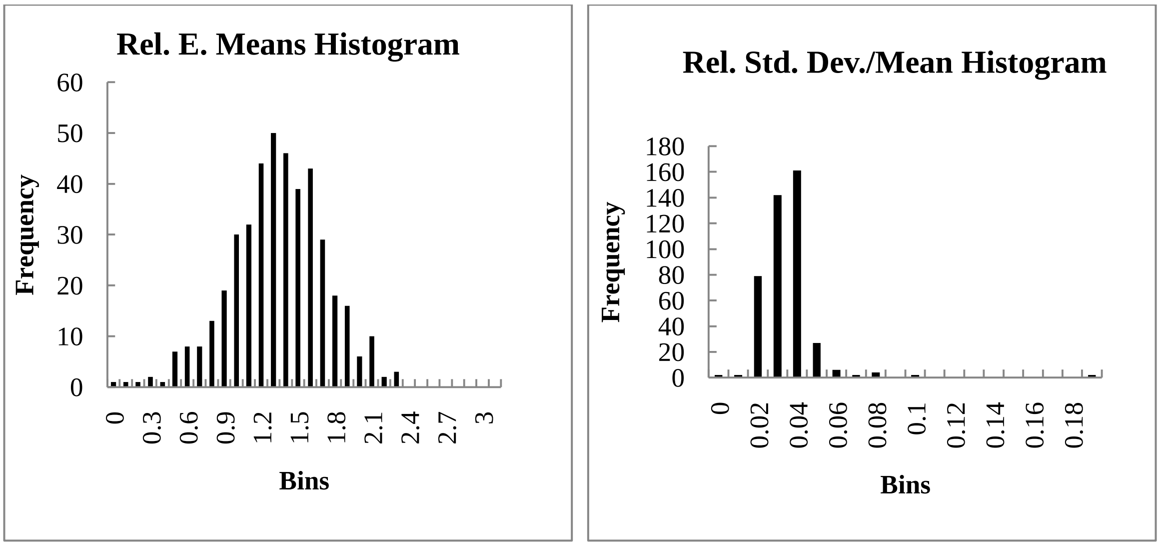

Figure 6.4. Relative energy means and relative energy standard deviation to mean ratio histograms for HF+ (depth 1)

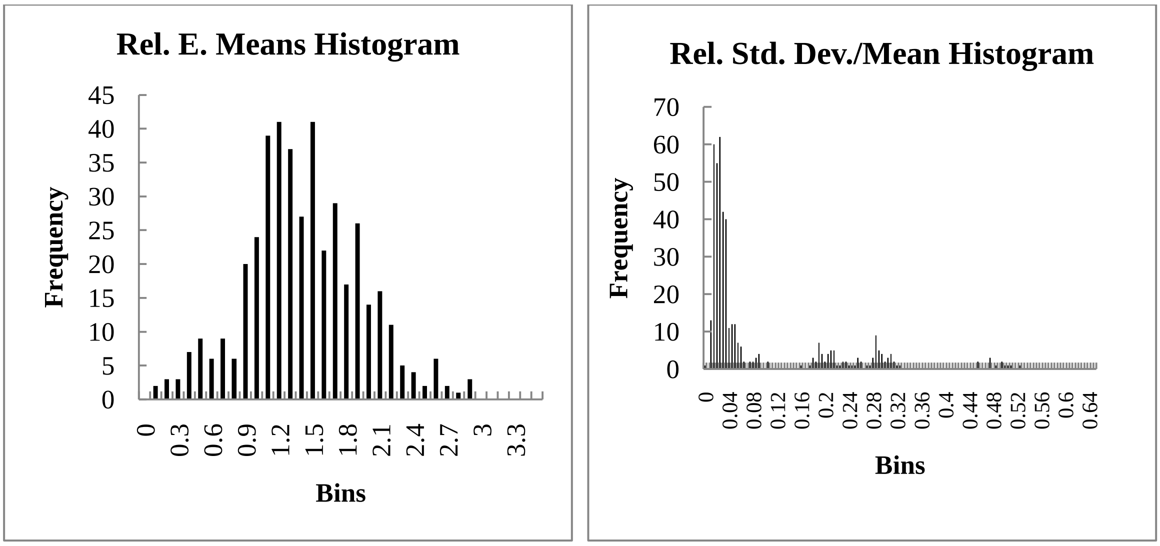

Figure 6.5. Relative energy means and relative energy standard deviation to mean ratio histograms for HF- (depth 1)

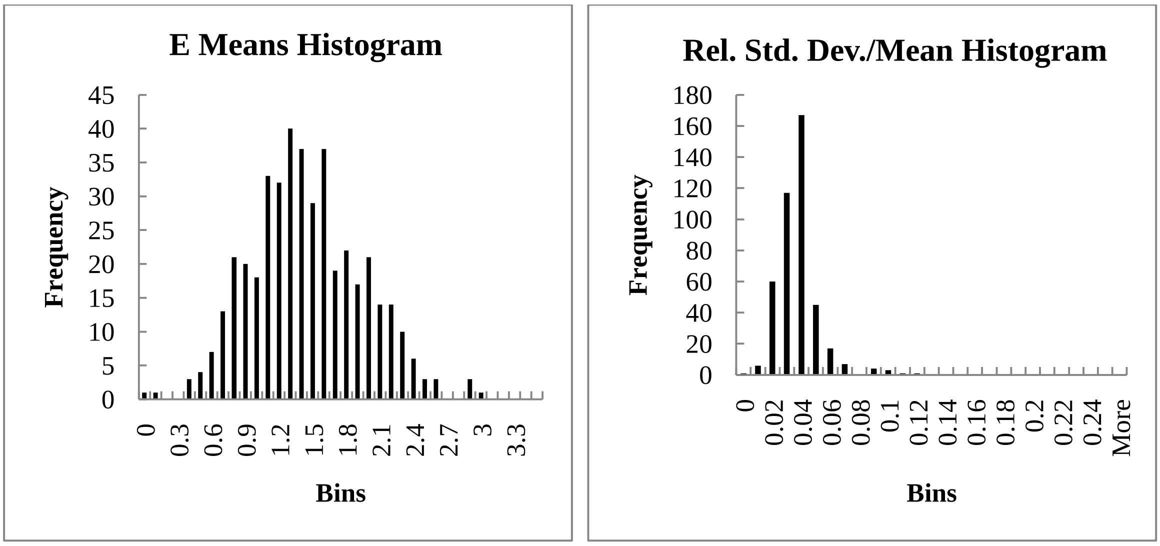

Figure 6.6. Relative energy means and relative energy standard deviation to mean ratio histograms for HF+ (depth 2)

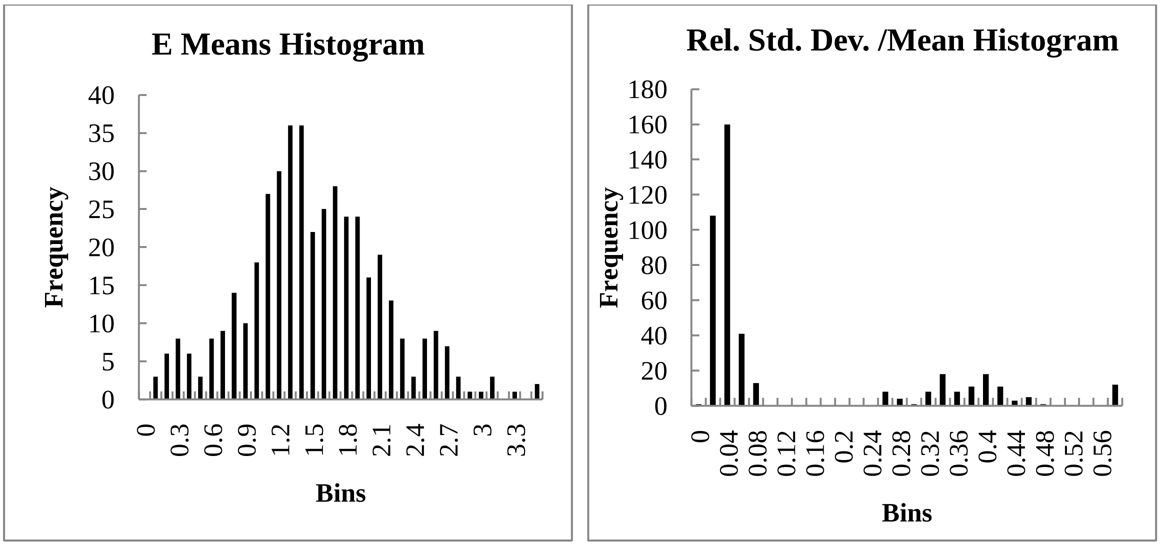

Figure 6.7. Relative energy means and relative energy standard deviation to mean ratio histograms for HF- (depth 2)

Table 6.2. Summary of the histograms

	Centroid	**Std. Dev.**	**Centroid**	**Std. Dev.**
	(Rel. E.)	(Rel. E.)	(Std.Dev/Mean)	(Std.Dev/Mean)
HF+ (depth 1)	1.33	0.38	0.033	0.010
HF- (depth 1)	1.42	0.51	0.027	0.012
HF+ (depth 2)	1.44	0.47	0.036	0.011
HF- (depth 2)	1.48	0.57	0.037	0.016

Carefully inspecting the energy histograms above, the energies that fall outside of the main peak were identified as problematic. The corresponding channels were examined more deeply.

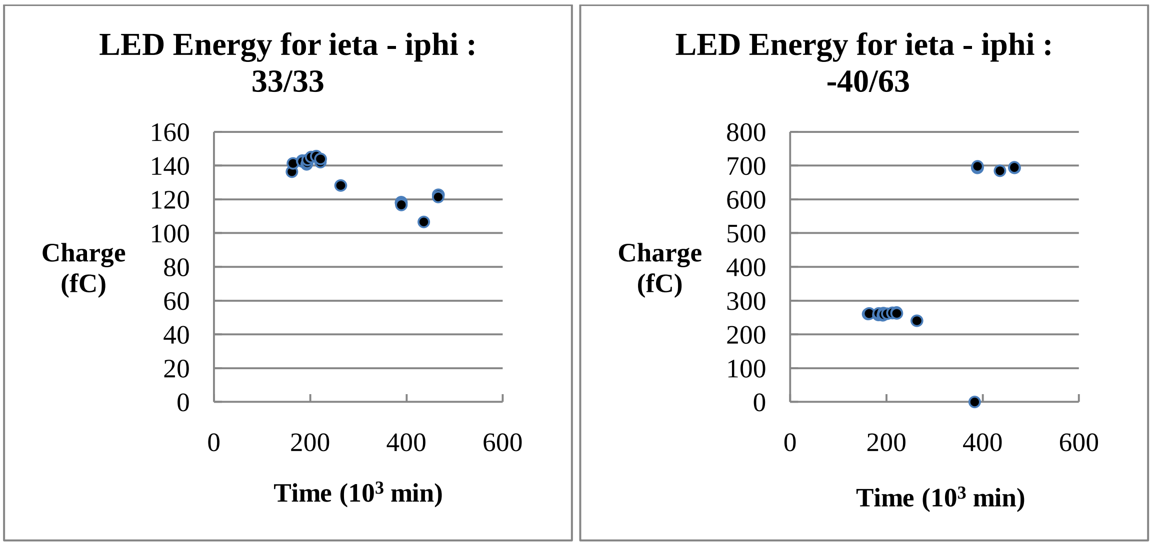

Figure 6.8. Energy distribution of 33/33 (depth 2) and -40/63 (depth 2) throughout 2009

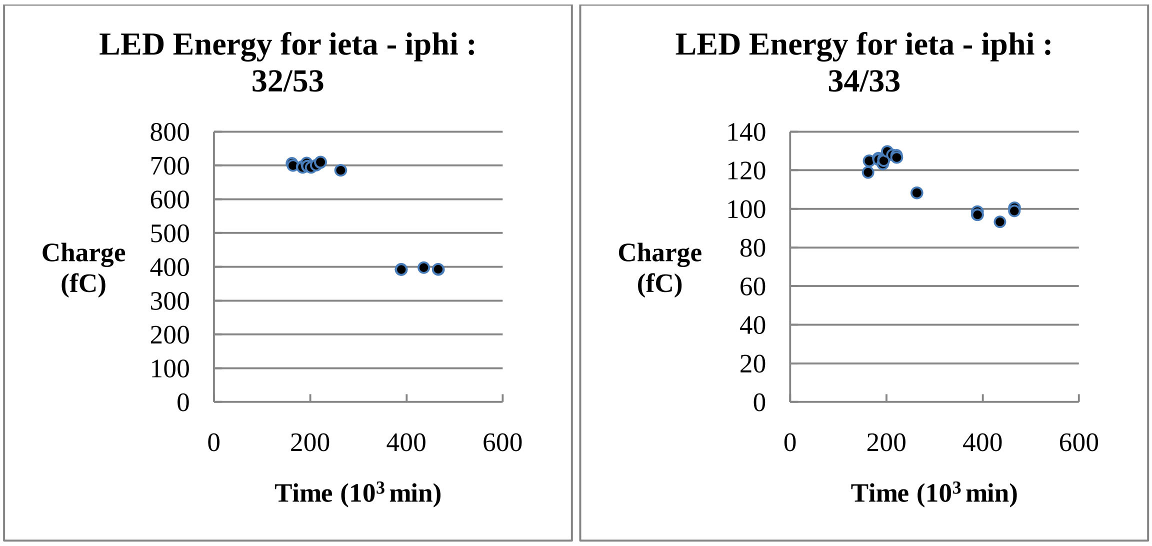

Figure 6.9. Energy distribution of 32/53 (depth 1) and 34/33 (depth 2) throughout 2009

Clearly, the energies have shifted down in September, in view of the Figures 6.8 and 6.9.

To see the global behavior, we plotted both relative mean energy and standard deviation/relative mean data in 3D. The 3D plots and the corresponding contour plots are given below in Figure 6.10.

Finally, the dependence of the energies on ieta and iphi alone was analyzed (Figures 6.12 through 6.15). Normally, the energies should have no dependence on iphi. However, for increasing ieta, energies should decrease, since the gains of the PMTs are lower (about $5x10^4$) for those that are close to the beam, and higher (10^5), for those that are further away, assuming there was no calibration correction for individual PMT gain.

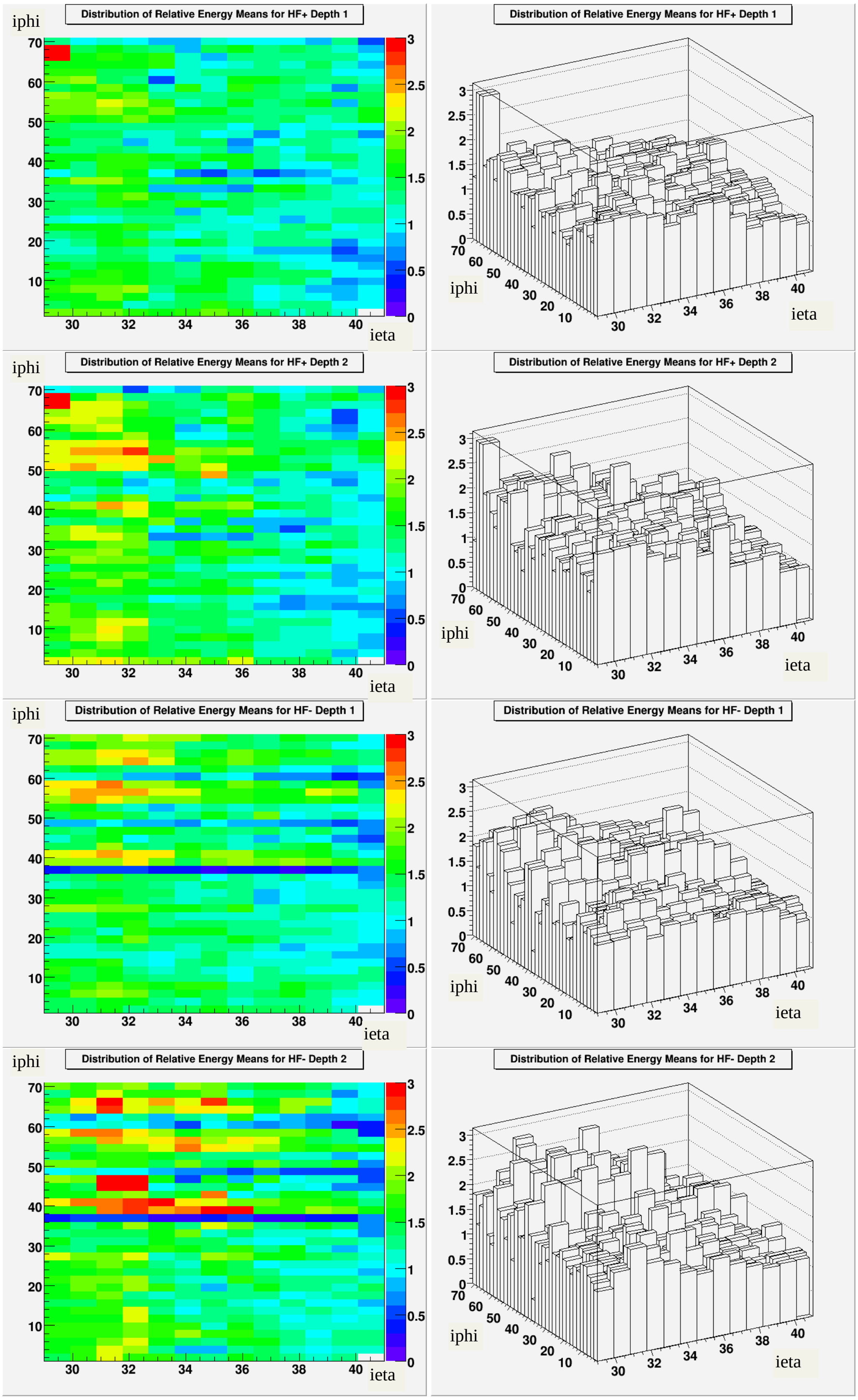

Figure 6.10. 3D and contour plots of relative energy means

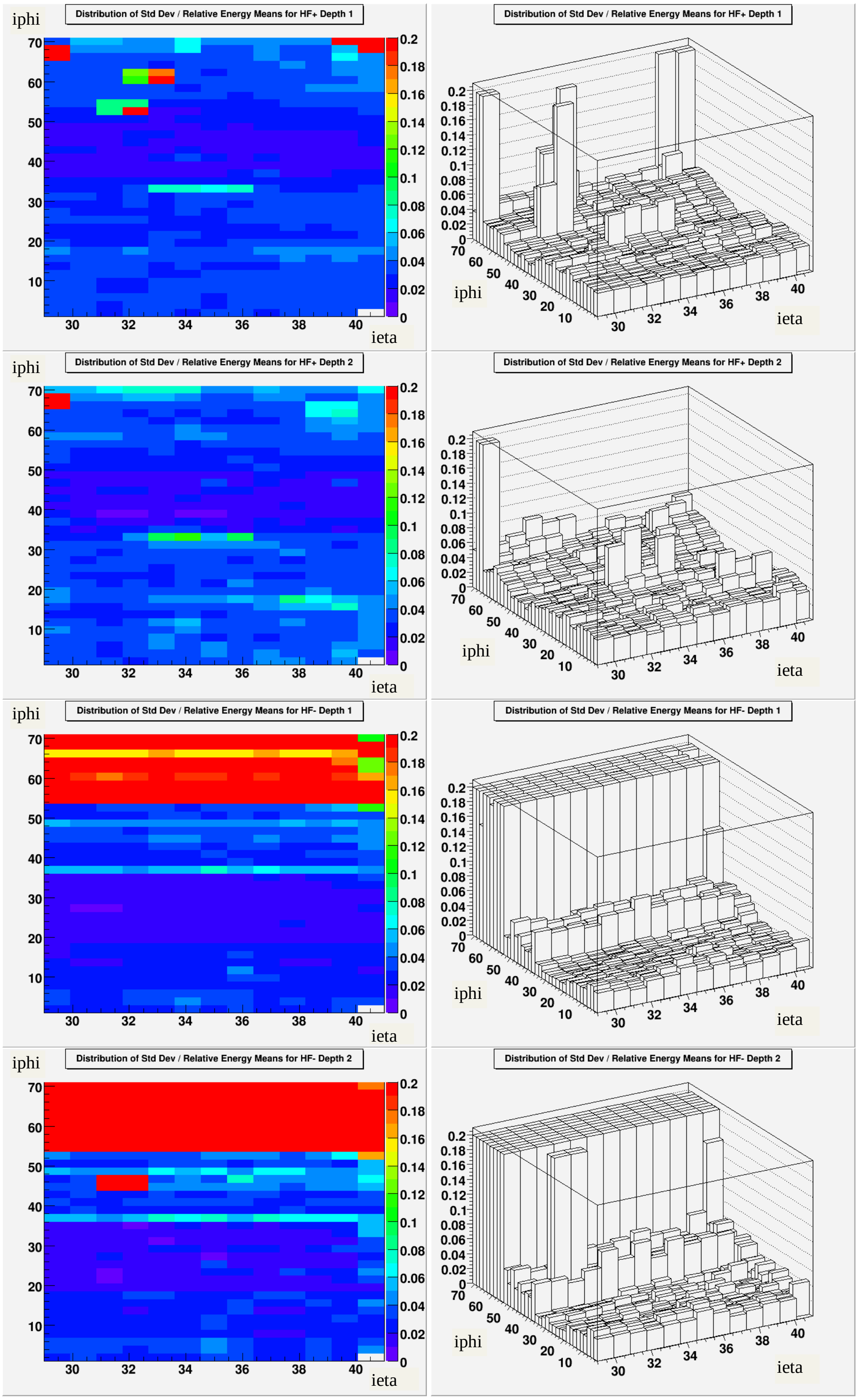

Figure 6.11. 3D and contour plots of relative energy standard deviation to energy means ratio

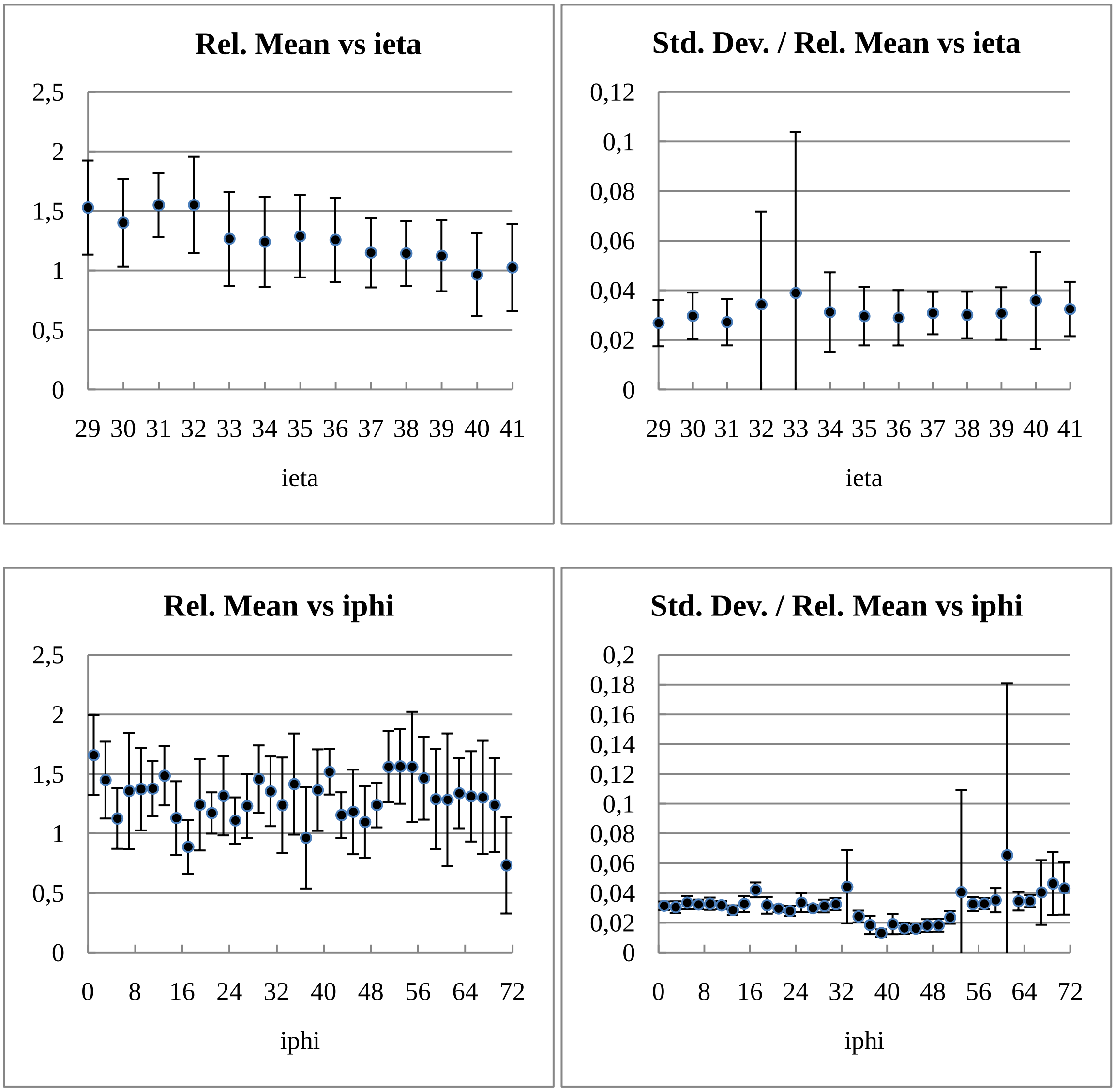

Figure 6.12. Ieta and iphi dependencies of the relative energy distributions for HF+ (depth 1)

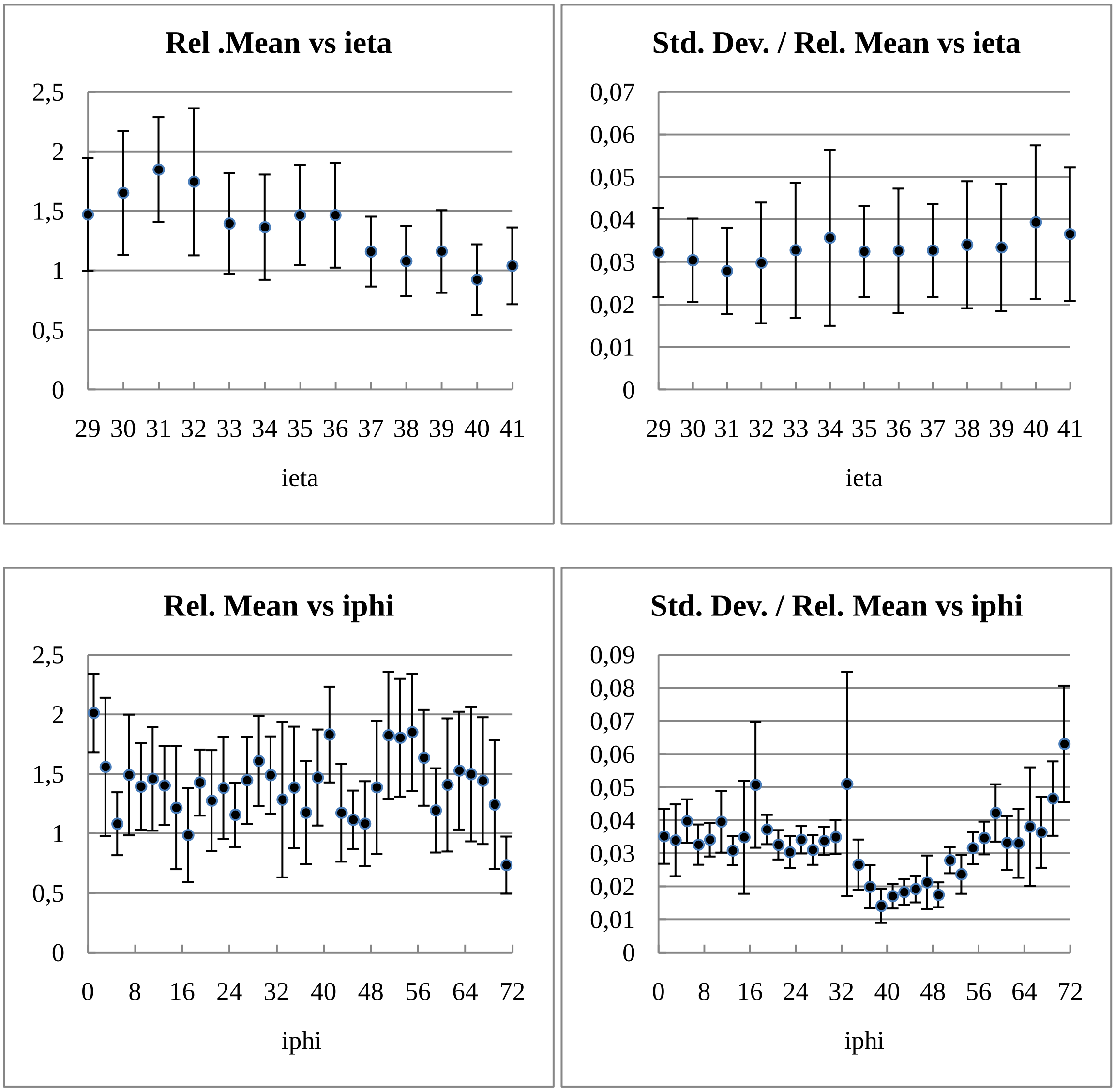

Figure 6.13. Ieta and iphi dependencies of the relative energy distributions for HF+ (depth 2)

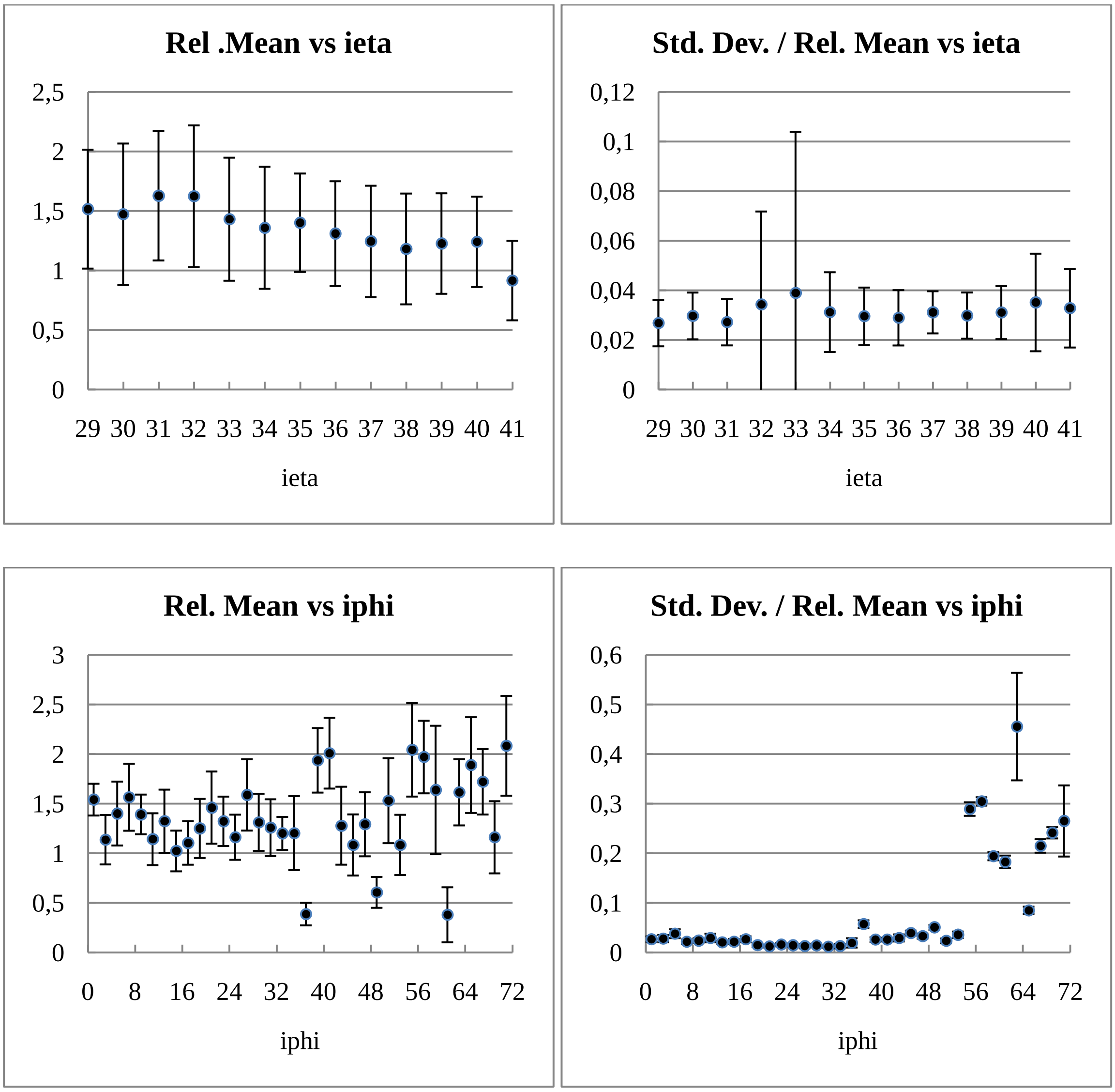

Figure 6.14. Ieta and iphi dependencies of the relative energy distributions for HF- (depth 1)

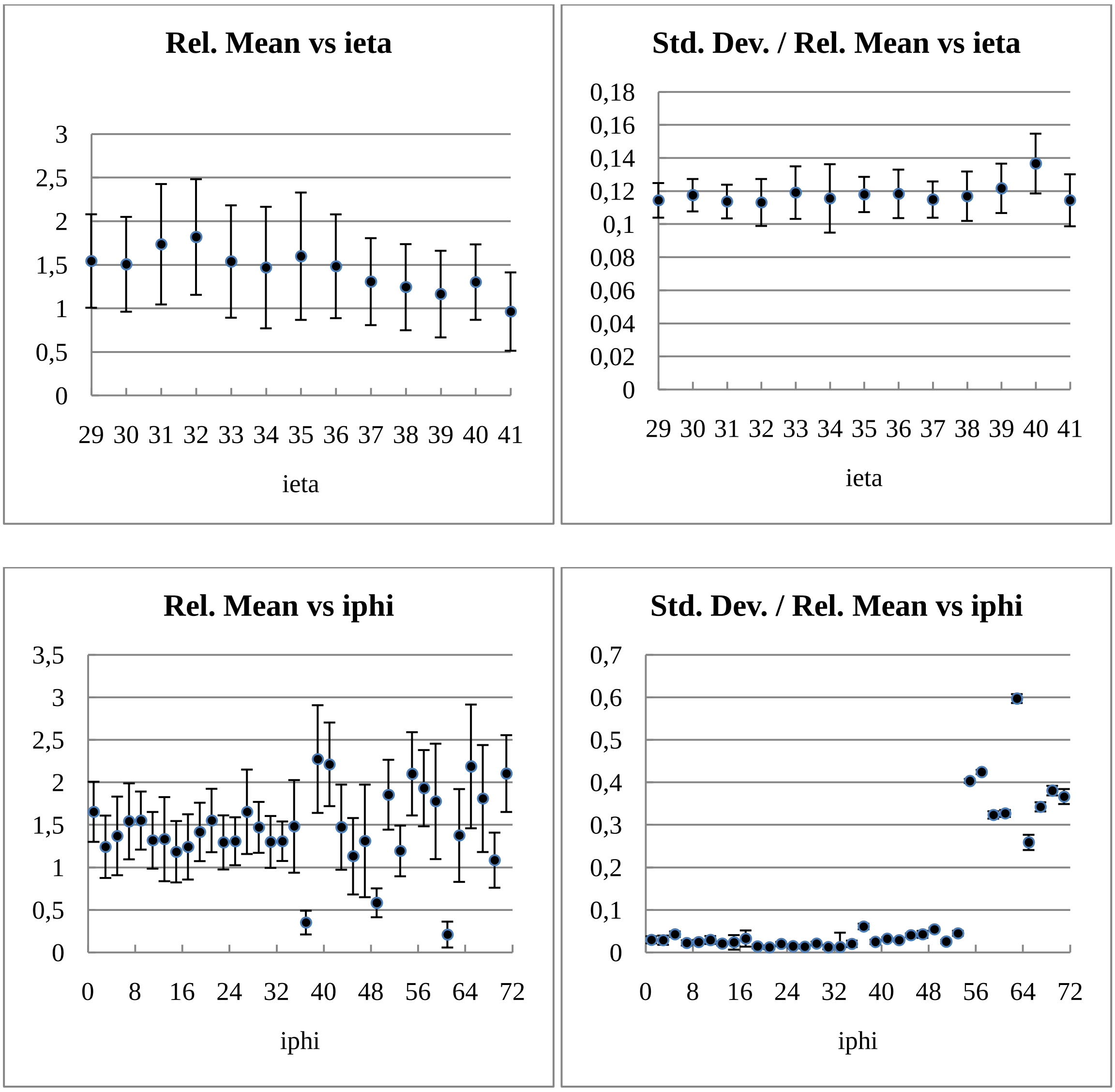

Figure 6.15. Ieta and iphi dependencies of the relative energy distributions for HF- (depth 2)

Since the energies in the channels had shifted down in runs after July 1, for the final part of the analysis, relative energy means and relative standard deviation to mean ratio histograms, 3D plots, contour plots, and relative mean vs. ieta or iphi plots were repeated, with the runs after 101915 being discarded.

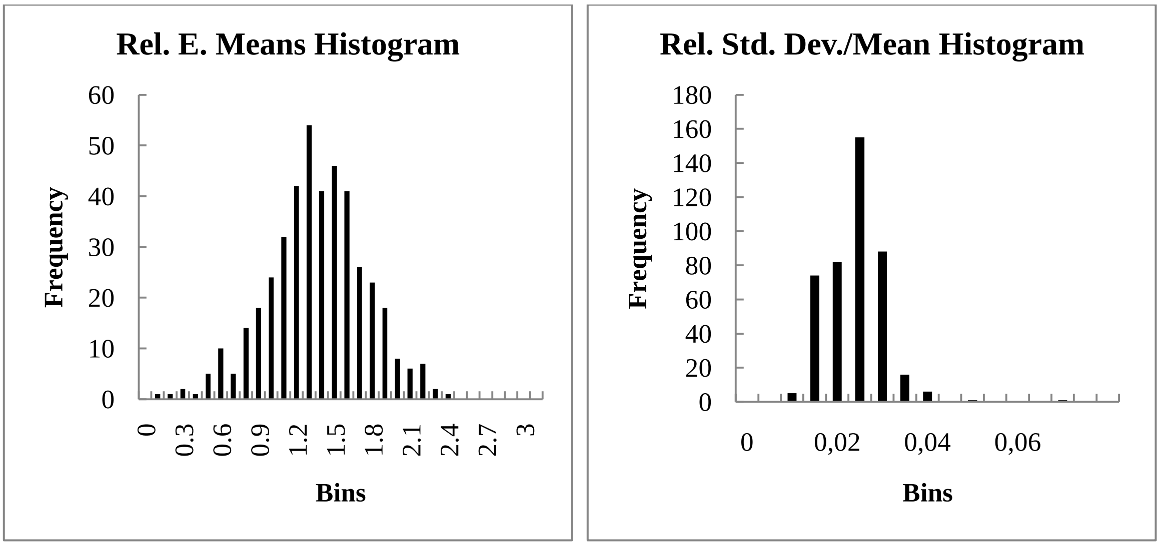

Figure 6.16. Relative energy means and relative energy standard deviation to mean ratio histograms for HF+ (depth 1)

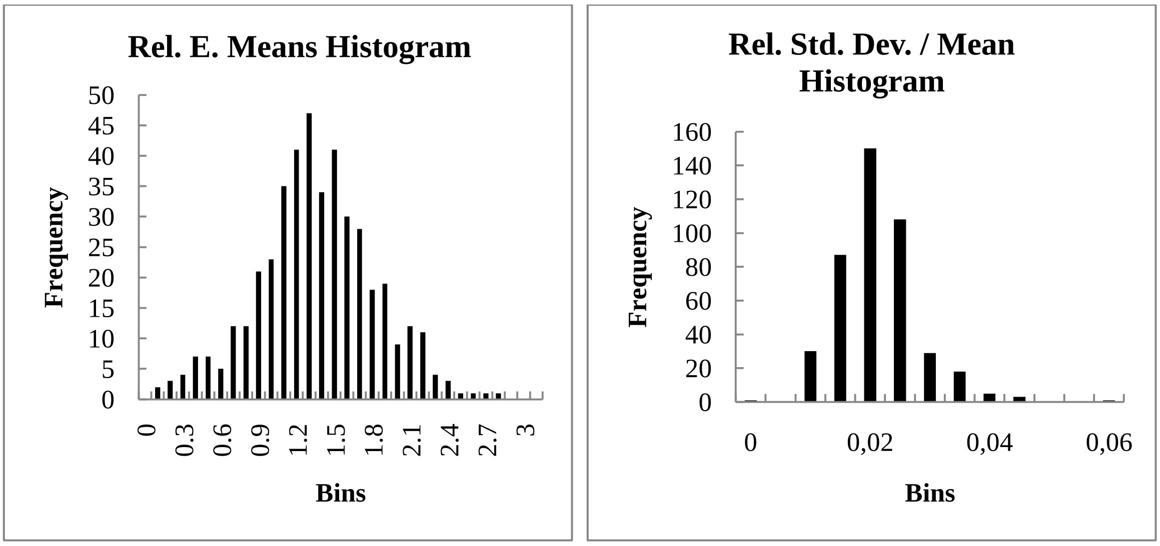

Figure 6.17. Relative energy means and relative energy standard deviation to mean ratio histograms for HF- (depth 1)

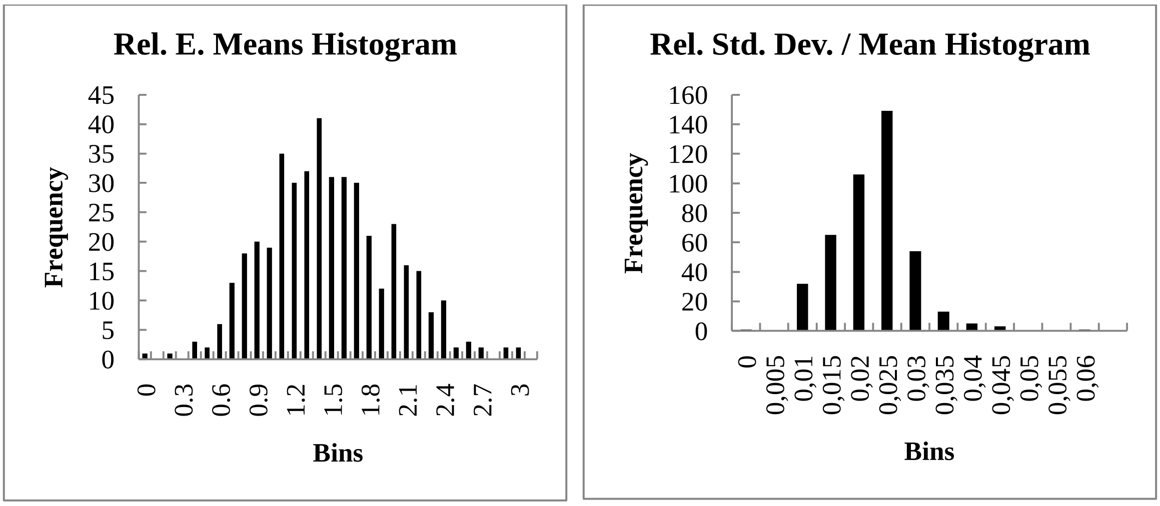

Figure 6.18. Relative energy means and relative energy standard deviation to mean ratio histograms for HF+ (depth 2)

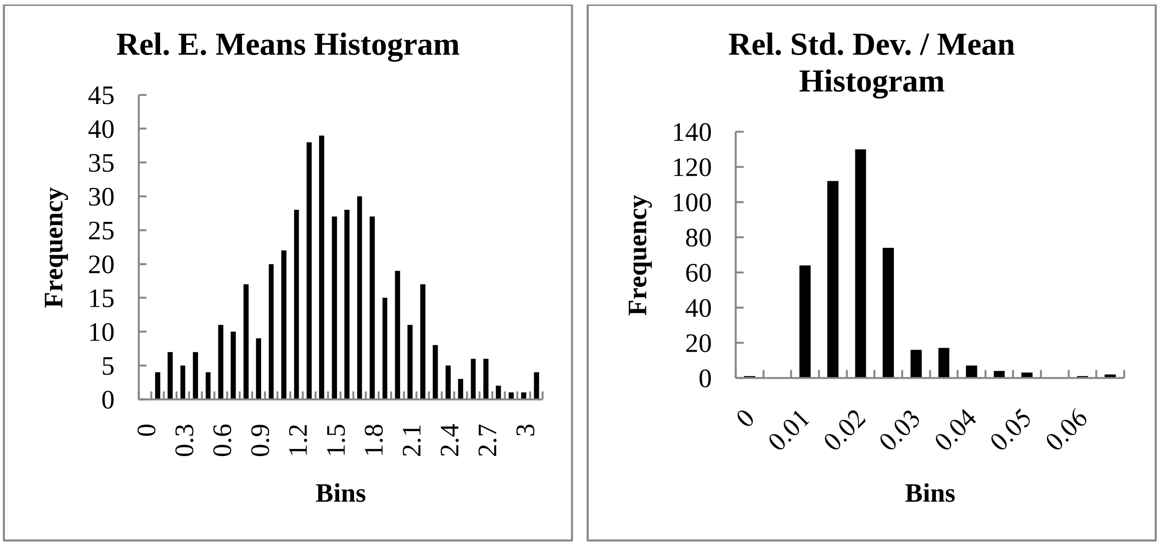

Figure 6.19. Relative energy means and relative energy standard deviation to mean ratio histograms for HF- (depth 2)

Table 6.3. Summary of the histograms without the runs after July 1

	Centroid	**Std. Dev.**	**Centroid**	**Std. Dev.**
	(Rel. E.)	(Rel. E.)	(Std.Dev/Mean)	(Std.Dev/Mean)
HF+ (depth 1)	1.36	0.39	0.024	0.006
HF- (depth 1)	1.35	0.45	0.021	0.007
HF+ (depth 2)	1.46	0.48	0.022	0.007
HF- (depth 2)	1.44	0.56	0.020	0.008

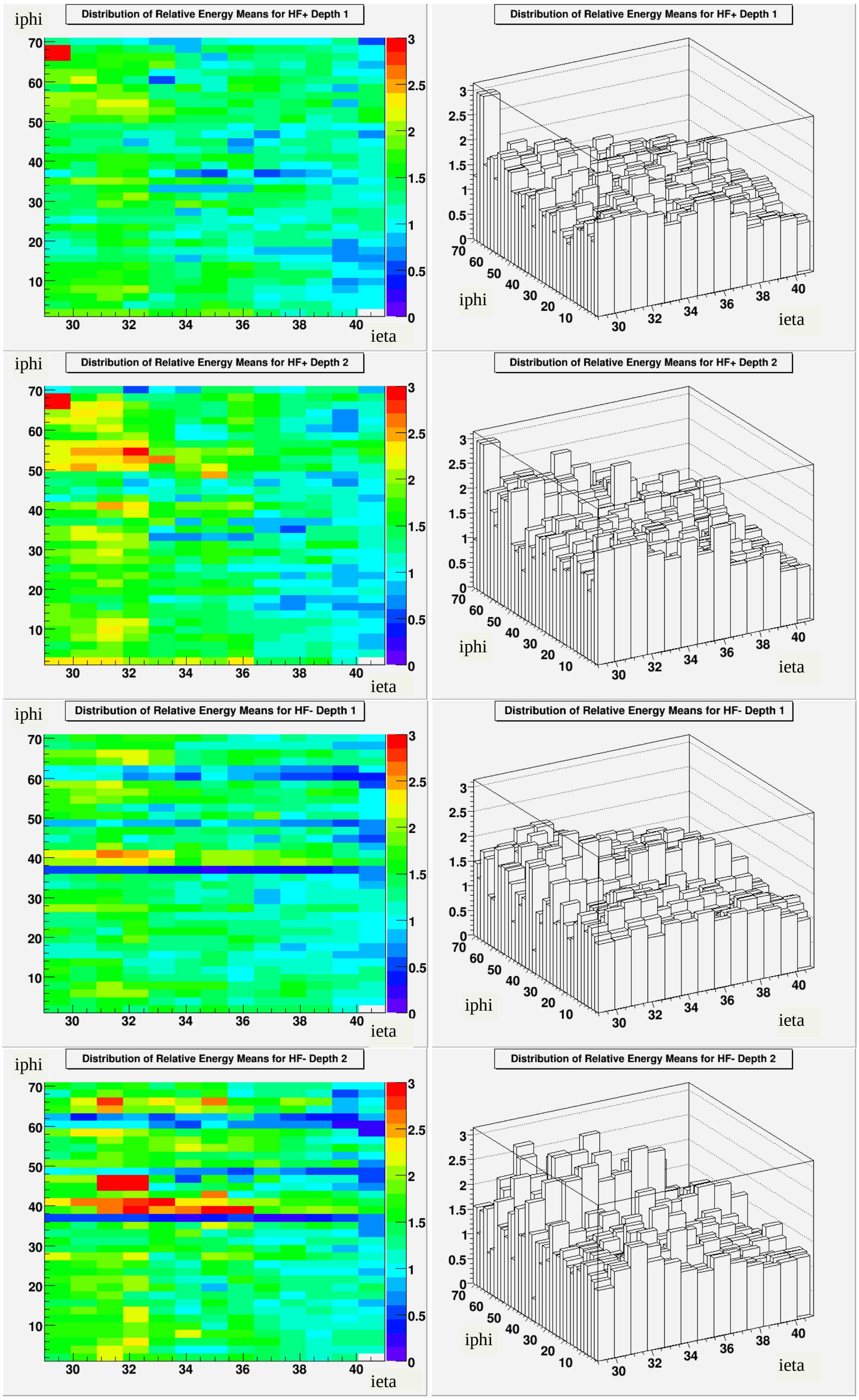

Figure 6.20. 3D and contour plots of relative energy means

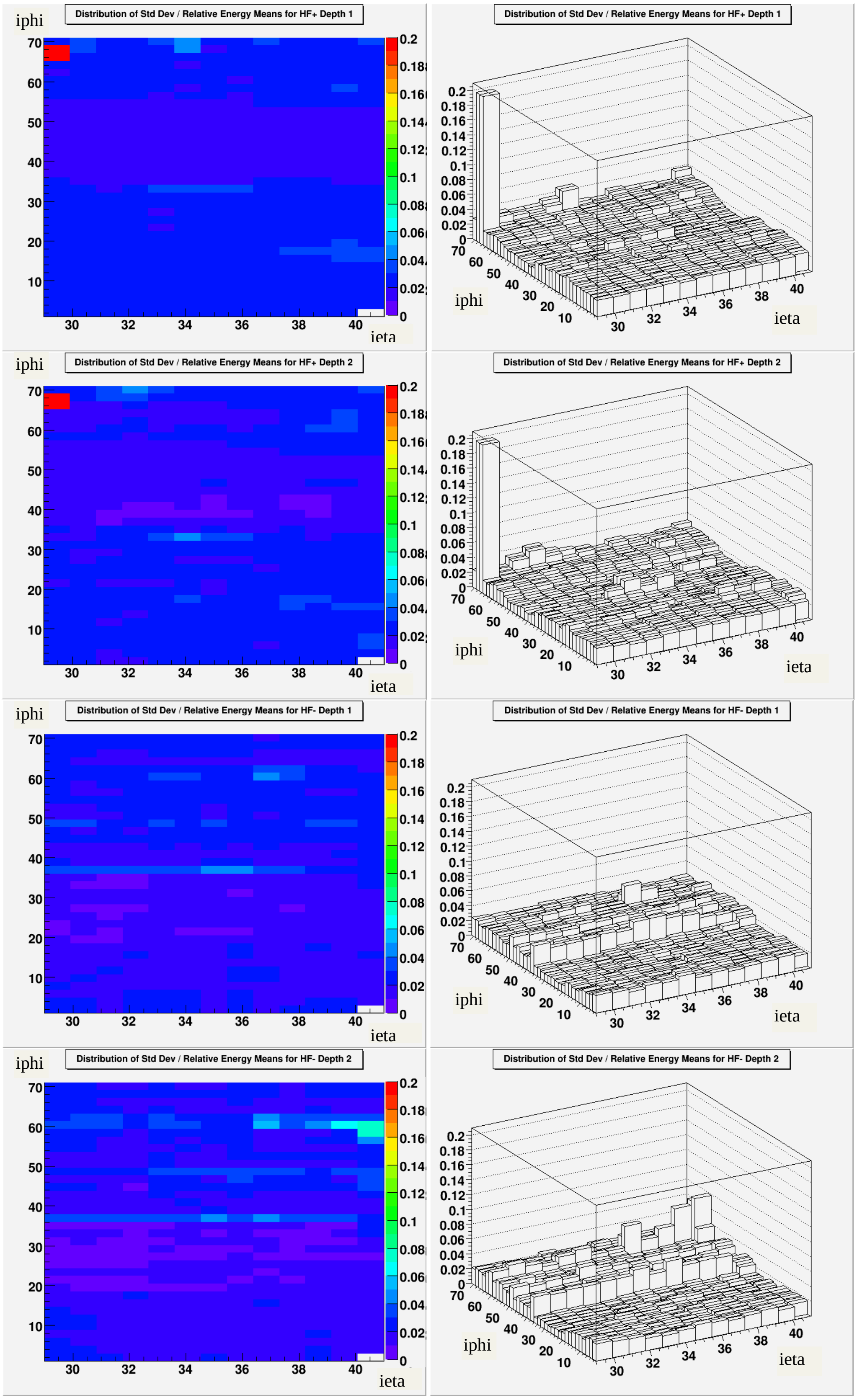

Figure 6.21. 3D and contour plots of relative energy standard deviation to energy means ratio

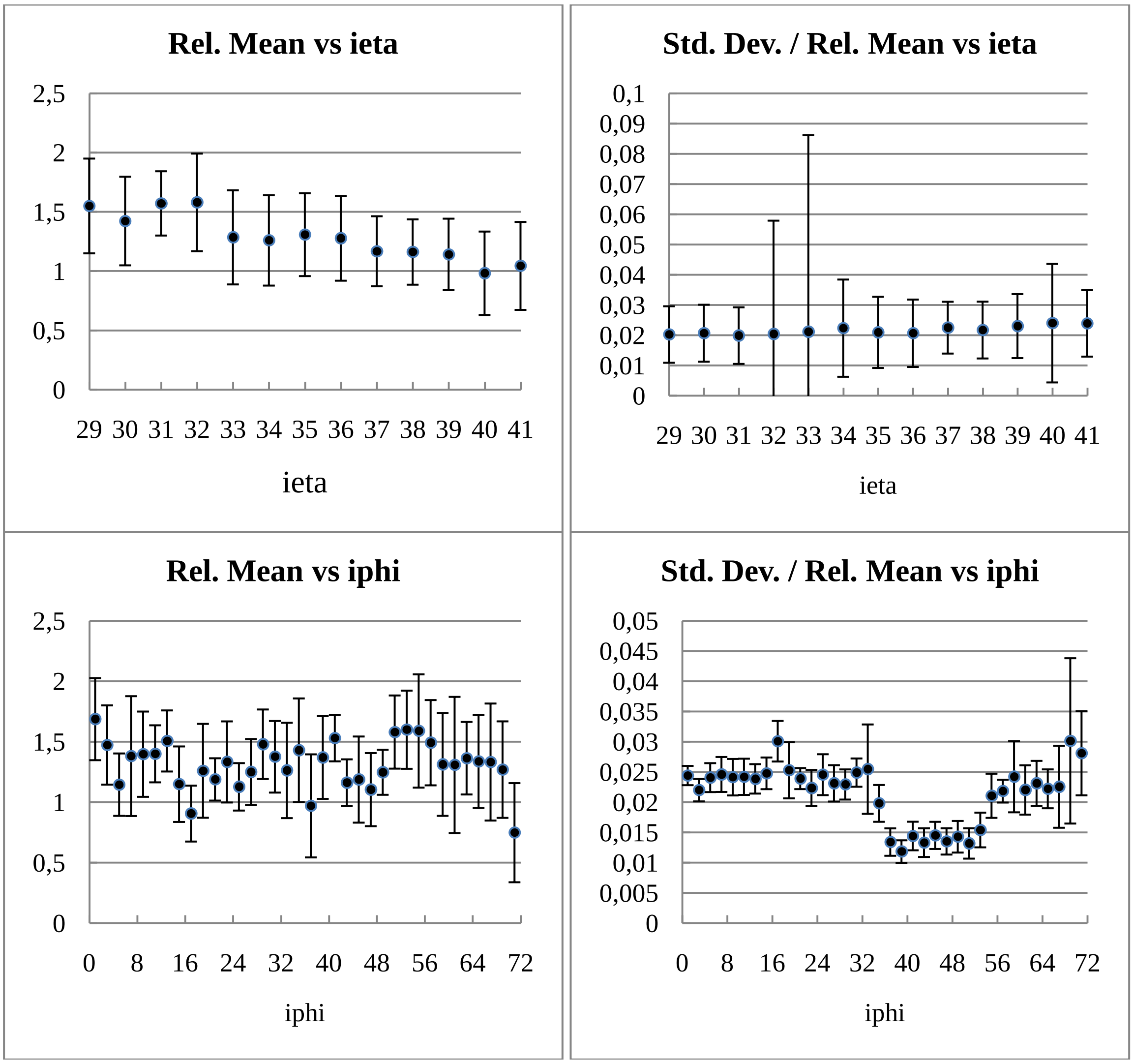

Figure 6.22. Ieta and iphi dependencies of the relative energy distributions for HF+ (depth 1)

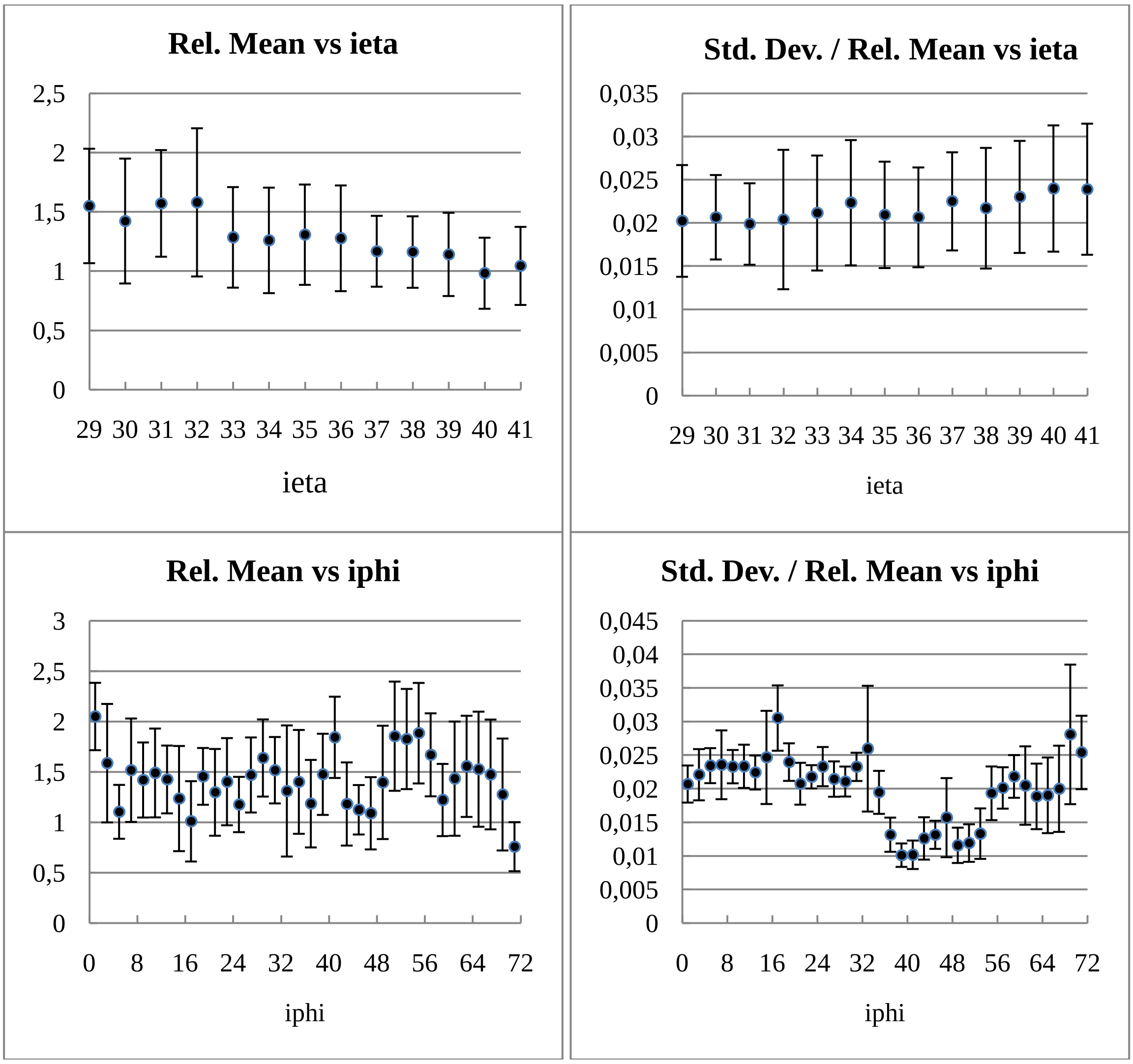

Figure 6.23. Ieta and iphi dependencies of the relative energy distributions for HF+ (depth 2)

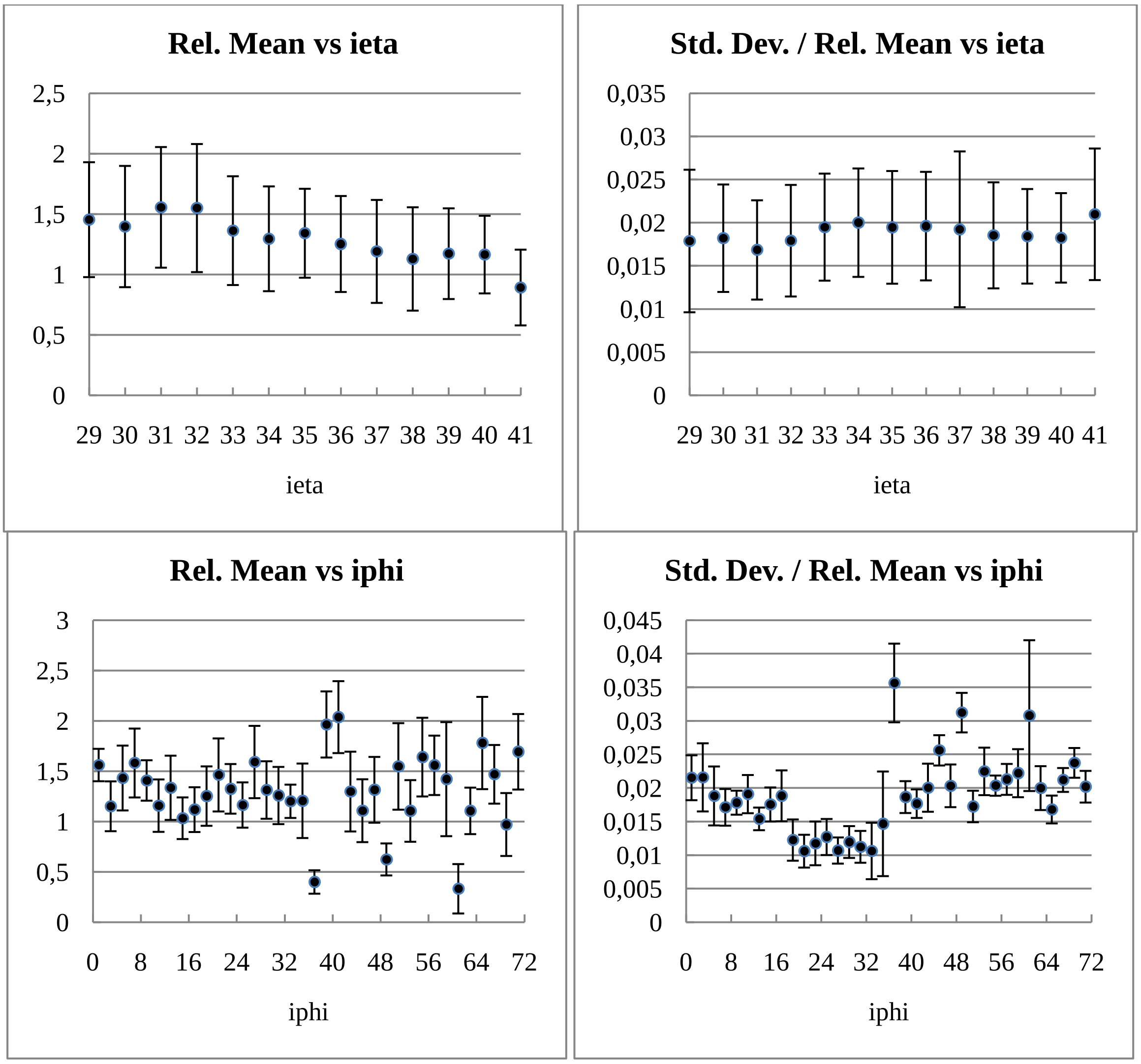

Figure 6.24. Ieta and iphi dependencies of the relative energy distributions for HF- (depth 1)

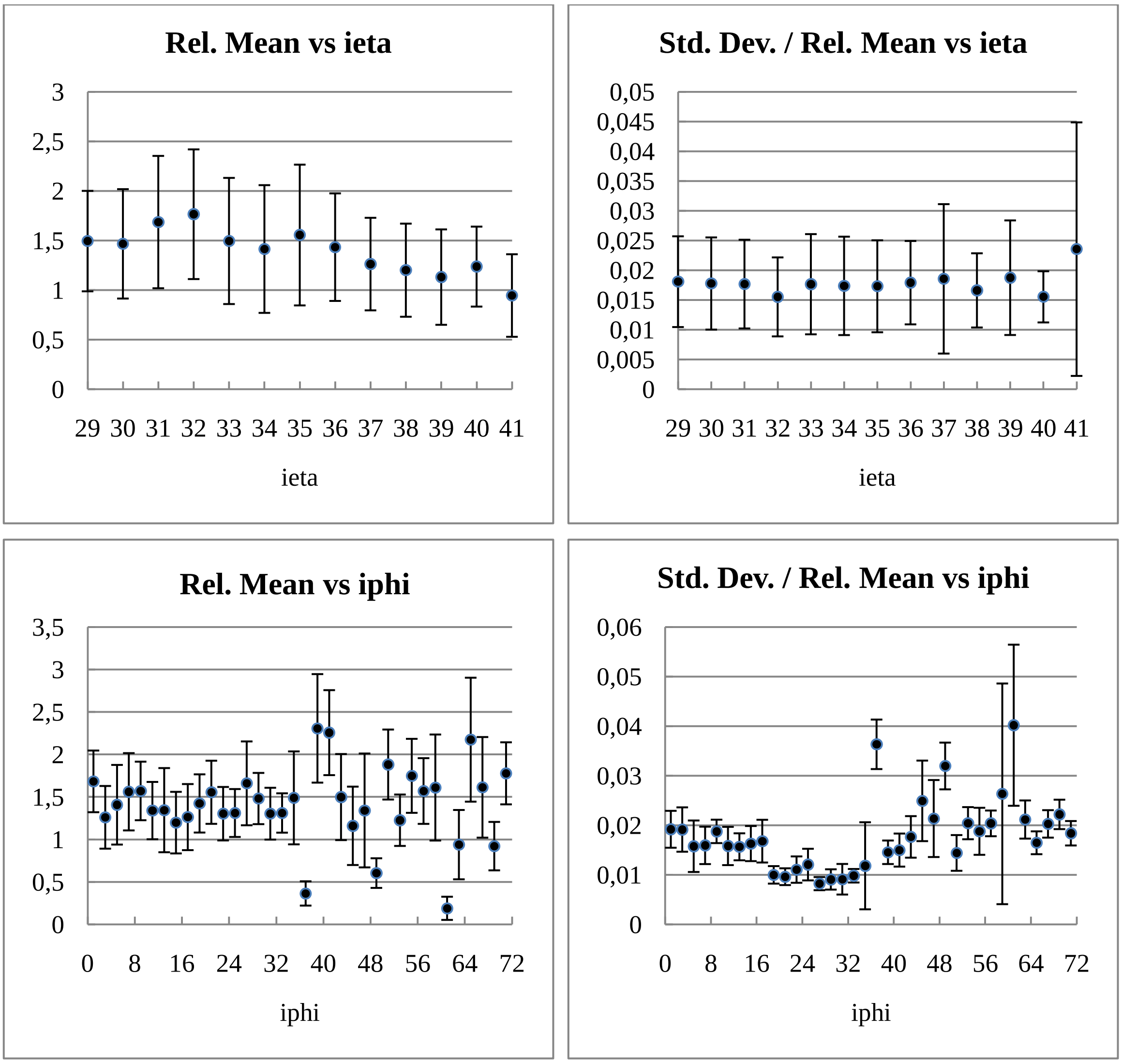

Figure 6.25. Ieta and iphi dependencies of the relative energy distributions for HF- (depth 2)

7. CONCLUSION

During the period when the detectors were in stable conditions, LED signals show a 2% fluctuation on the average. Energies reported due to the LED light also show a variation of 35% (one sigma) around the mean.

Viewing all the channels in a two dimensional color plot easily compares the channels. By looking at such plots of the relative energies averaged over the final set of runs, one can spot the channels with possible problems. In HF-, there seem to be three bands corresponding to iphi values 37, 49 and 61+63. These three bands with very low signals show up both in depth 1 and 2. However, adjacent iphi channels seem to be at a much higher energy. (This could be due to some mismatch in the optical coupling of the LED fibers in these regions or the light distribution.) On the other hand, in HF+, there are no such band-like regions, but a region with high energy values appear around ieta: 29-32 and iphi: 50-67. There were also low signals observed in iphi 33 mid ieta values. On April 26 2010, there was an intervention to the LED system, in view of the peculiar signals from iphi 33. After replacing the relevant RBXs, the signals went back to normal levels. There may be a similar problem in iphi 37 region also.

When we look at the same plots in our initial analysis where we included the runs after July 1, it appears that most of the problematic areas mentioned above are still there. There is not much change as expected, since adding four runs with shifted energies does not change the overall behavior too much. However, when we look at the same type of plots for the relative energy standard deviations divided by the relative energy mean, we see a drastic change especially in HF- at iphi values above 53 (which corresponds to HF-Quadrant 4). In HF+, there are a couple of areas with very large fluctuations.

We also observed that the channels 29/67 in HF+ (Depth 1 and Depth 2) and 32/45 in HF- (Depth 2) are dead. Also, 41/71 in HF+ (Depth 1) seems to be registering only noise.

According to the electronic logbook, on August 18 2008, crystals were installed in HF+ at the following channels (ieta / iphi / long or short fibers) : 30/67 S (BGO), 37/67 L (BGO), 38/67 S (BGO), 32/67 S (LYSO), 35/67 L (LYSO), 36/67 S (LYSO). Also, channel 29/67 (both long and short fibers) was taped (PMT faces were covered). This is the reason for our observation about the channel 29/67 being dead. However, for the above mentioned channels with crystals, we did not observe any noticable different behavior.

The relative energy means are a combination of the PMT gain and the LED light intensity. As a next step, we are planning to remove the contribution coming from the PMT gain. It will be a more direct way of analyzing the gain stability.

Despite certain exceptions described above, the LED system is stable within 2% according to the 2009 data.

REFERENCES

1. Acosta, D., Michel Della Negra, L. Foà, A. Hervé, Achille Petrilli, *CMS Physics : Technical Design Report Volume 1 : Detector Performance and Software,* CMS Collaboration, 2006.

2. http://lhc-machine-outreach.web.cern.ch/lhc-machine-outreach/components/magnets/types_of_magnets.htm

3. http://public.web.cern.ch/press/PressReleases/Releases2010/PR07.10E.html

4. LHC Experiments Committee, LHCC, “The Muon Project Technical Design Report”, CERN/LHCC 97-32 CMS TDR 3, CMS Collaboration, 1997.

5. Griffiths, D., *Introduction to Elementary Particles, Second Edition,* WILEY-VCH Verlag GmbH & Co. KgaA, Weinheim, 2008.

6. Zwicky, F., "Die Rotverschiebung von extragalaktischen Nebeln", Helvetica Physica Acta 6: 110–127, 1933.

7. Zwicky, F., "On the Masses of Nebulae and of Clusters of Nebulae", Astrophysical Journal 86: 217, 1937.

8. Rubin V. and W. K. Ford, Jr, "Rotation of the Andromeda Nebula from a Spectroscopic Survey of Emission Regions", Astrophysical Journal 159: 379, 1970.

9. Rubin V., N. Thonnard, W. K. Ford, Jr, "Rotational Properties of 21 Sc Galaxies with a Large Range of Luminosities and Radii from NGC 4605 (R=4kpc) to UGC 2885 (R=122kpc)", Astrophysical Journal 238: 471, 1980.

10. Griest K., *The Search for Dark Matter: WIMPs and MACHOs*, Review Talk, March 1993.

11. Fabjan, Christian W. and Fabiola Gianotti, *Calorimetry For Particle Physics*, Reviews of Modern Physics, Volume 75, October 2003.

12. Akgun U., E. W. Anderson, A. S. Ayan, E. Gülmez, M. Miller, Y. Onel, I. Schmidt and D. Winn, “Comparison of PMTs From Three Different Manufacturers for the CMS-HF Forward Calorimeter”, IEEE Transactions On Nuclear Science, 51, (2004)1909, 2004.

13. Gülmez E., U. Akgun, A. S. Ayan, P. Bruecken, F. Duru, A. Mestvirishvili, M. Miller, J. Olson, Y. Onel, I. Schmidt, E. W. Anderson and D. Winn, “Selection and Testing of 2000 Photomultiplier Tubes for the CMS-HF Forward Calorimeter”, Proceedings of IMTC 2004 Instrumentation and Measurement Technology Conference, Como, Italy, May 18-20, (2004) 1870, 2004.

14. Akgun U., A. S. Ayan, P. Bruecken, F. Duru, E. Gülmez, A. Mestvirishvili, M. Miller, J. Olson, Y. Onel, I. Schmidt, “Complete Tests of 2000 Hamamatsu R7525HA Phototubes for the CMS-HF Forward Calorimeter”, Nucl. Instr. And Meth. A550, 145(2005), 2005.

15. Abdullin S. et al, “Design, Performance, and Calibration of CMS Forward Calorimeter Wedges”, CMS HCAL Collaboration, Eur. Phys. J. C 53, 139-166 (2008), 2008.

16. Brun R. et al., *Root User’s Guide 5.24,* CERN, 2009.